# Imaging and Forecasting of Ionospheric Structures and Their System Impacts

Bodo Reinisch
Gary Sales
Paul Song


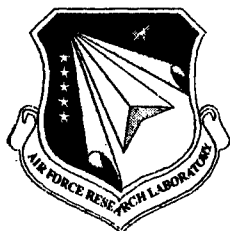University of Massachusetts Lowell
Center for Atmospheric Research
600 Suffolk Street
Lowell, MA 01854

January 2005

Scientific Report No. 2

**20050725 024**

**AIR FORCE RESEARCH LABORATORY**
Space Vehicles Directorate
29 Randolph Rd
**AIR FORCE MATERIEL COMMAND**
Hanscom AFB, MA 01731-3010

This technical report has been reviewed and is approved for publication.

/signed/                                          /signed/

GLEN L. MARPLE, SMSgt                    JOEL B. MOZER, Chief
Contract Manager                              Space Weather Center of Excellence

# REPORT DOCUMENTATION PAGE

| 1. REPORT DATE (DD-MM-YYYY) | 2. REPORT TYPE | 3. DATES COVERED (From - To) |
|---|---|---|
| 01-27-2005 | Scientific Report No. 2 | 1 October 2003-30 September 2004 |

| 4. TITLE AND SUBTITLE | 5a. CONTRACT NUMBER |
|---|---|
| Imaging and Forecasting of Ionospheric Structures and Their System Impacts | F19628-02-C-0092 |
| | **5b. GRANT NUMBER** |
| | **5c. PROGRAM ELEMENT NUMBER** |

| 6. AUTHORS | 5d. PROJECT NUMBER |
|---|---|
| Bodo Reinisch, Gary Sales, Paul Song | 2311 |
| | **5e. TASK NUMBER** SD |
| | **5f. WORK UNIT NUMBER** ^AD |

| 7. PERFORMING ORGANIZATION NAME(S) AND ADDRESS(ES) | 8. PERFORMING ORGANIZATION REPORT NUMBER |
|---|---|
| University of Massachusetts Lowell Center for Atmospheric Research 600 Suffolk St. Lowell, MA 01854 | |

| 9. SPONSORING/MONITORING AGENCY NAME(S) AND ADDRESS(ES) | 10. SPONSOR/MONITOR'S ACRONYM(S) |
|---|---|
| Air Force Research Laboratory 29 Randolph Rd Hanscom AFB, MA 01731-3010 Contract Manager: SMSgt Glen L. Marple | |
| | **11. SPONSOR/MONITOR'S REPORT NUMBER(S)** AFRL-VS-HA-TR-2005-1036 |

**12. DISTRIBUTION/AVAILABILITY STATEMENT**
Approved for public release; distribution unlimited

**13. SUPPLEMENTARY NOTES**

**14. ABSTRACT**

The COPEX attention was focused on the details of the early stages in the development of ionospheric (F-region) instabilities that precede the growth of equatorial bubbles. We continued our work on ground VLF station monitoring with the RPI/IMAGE instrument. We carried out RPI measurements using specifically designed operational modes with lower receiver gains. In the past year, several Radiation Belt Remediation (RBR) studies were done and many of them remain active. The results of two HAARP heating experiments with the digisonde at Gakona, Alaska are described.

Additionally, we discuss work done in several areas. We introduced a new Java-based Drift software package for the digisonde drift data analysis and visualization. DISS Support for the Digisonde Network continued. The CAL/VAL, project which involved the establishment of a substantial database from a global network of digisondes, is described. Product and the improvements offered by ARTIST 4.5 are discussed.

**15. SUBJECT TERMS**
Spread F, COPEX, RPI/IMAGE, Equatorial Ionosphere, Whistler Waves, VLF transmissions, Plasma Sheath, Ray Tracing, Radiation Belt Remediation, LORERS, Plasmasphere, HAARP, Cal/Val, Drift Software, ARTIST 4.5

| 16. SECURITY CLASSIFICATION OF: | | | 17. LIMITATION OF ABSTRACT | 18. NUMBER OF PAGES | 19a. NAME OF RESPONSIBLE PERSON |
|---|---|---|---|---|---|
| a. REPORT | b. ABSTRACT | c. THIS PAGE | | | SMSgt Glen L. Marple |
| UNCL | UNCL | UNCL | UNL | 78 | **19B. TELEPHONE NUMBER** (Include area code) (781) 377-3151 |

# CONTENTS

# FIGURES

# TABLES

# 1    INTRODUCTION

For the past year, the University of Massachusetts Center for Atmospheric Research (UMLCAR) has been active in a variety of areas in support of this AFRL contract entitled "IMAGING AND FORECASTING OF IONOSPHERIC STRUCTURES AND THEIR SYSTEM IMPACTS." Several of these areas are discussed briefly in this introduction and eight subjects are presented in greater detail in the subsequent sections of this report. The detailed presentations are:

## 1.1    COPEX - Equatorial Scintillation

Following the analysis of the COPEX campaign data presented in the previous annual report, attention was turned towards the details of the early stages in the development of ionospheric (F-region) instabilities that precede the growth of equatorial bubbles. For this investigation, ionograms from Jicamarca, Peru, Cachimbo and Sao Luis, Brazil were examined over two time periods to determine which days were quiet (no satellite traces on the ionograms, no spread F and no bubbles) and which days were active. The time intervals used here were first the COPEX campaign (1 October through 9 December 2002) and then the sixty-day period from March through April 2003. The second period was chosen because during that time the solar declination was the conjugate of the solar declination during the COPEX campaign period.

## 1.2    VLF Station Observations

In the frame of the present project we continued our work on ground VLF station monitoring with the Radio Plasma Imager (RPI) instrument on the IMAGE spacecraft. As reported in our 2003 annual report we had been able to successfully identify transmissions from ground-based VLF stations using the retrospective analysis of our 2001-2002 observations. In 2003-2004 we carried out RPI measurements using specifically designed operational modes with lower receiver gains. Statistical analysis of the data obtained made it possible to confirm the validity of the suggested model for the VLF signal propagation and to estimate the main characteristics of this process.

1

## 1.3 VLF Induced Electron Pitch Angle Scattering (IEPAS)

The objective of this investigation is to use manmade Very-Low Frequency (VLF) waves to stimulate the wave-particle interaction in the radiation belt. The results of the enhanced interaction, if successful, would substantially reduce the lifetime of the relativistic electrons in the belt by pitch-angle diffusion of the particles into the atmosphere. In the past year, several studies were carried out and many of them remain active. They include the concept study of the Low-earth Orbit Relativistic Electron Remediation System (LORERS), planning studies for a transmitter on the Cygnus mission, a trade-off study of a capacitance-loaded antenna, operation and data analyses of RPI monitoring ground-based VLF transmitters, and RPI experiments of whistler wave transmission. All these studies provide significant knowledge for the feasibility of the IEPAS concept. In this report we summarize our results in terms of scientific issues because the physical understanding can be applied to different mission scenarios by using corresponding parameters.

## 1.4 HAARP Campaign

During two HAARP heating experiments on 22 and 23 March 2004 extending from 23 UT until about 04 UT the digisonde at Gakona, Alaska operated in the ionogram and "drift" mode in cooperation with other radar and optical observations. In this drift mode, the digisonde is able to detect the spatial (horizontal) distribution of ionospheric (F-region) irregularities using the so-called skymap format. During both campaigns the HAARP heater was operated on a 5-minute on and 10-minute off cycle at an RF frequency that varied as the F-layer critical frequency changed.

## 1.5 Drift software development

We introduced a newly developed conceptual Java-based software package for the digisonde drift data analysis and visualization. This package will replace the less versatile Fortran-based applications developed by the UMLCAR earlier. A dedicated Drift

Database (DriftBase) intended for raw and processed drift data storage, access and exchange has also been established and is presented in this report.

## 1.6 DISS Support for Digisonde Network

The work this year as described in more detail below focused on support in several different areas. Security was one area where numerous Air Force AFCERTS/TCNO's and Microsoft Security Bulletins were analyzed for applicability to the DISS. In general, most of the applicable patches could be applied in a straightforward manner. Support for shipments and deployments in Kwajalein and Boulder took place. Additional work involved a study of the feasibility or difficulty to upgrade the Operating System of the DISS Artist4 computer from Windows NT 4.0 to Windows XP. Additionally, a new DPS-4 was constructed as an upgrade for the HAARP digisonde.

## 1.7 CAL/VAL Project

This project involves the establishment of a substantial database from a global network of digisondes to support the evaluation of the SSUSI (limb scanning ultraviolet imager / spectrometer) and SSULI (nadir scanning ultraviolet imager /spectrometer and photometer) measurements from the DMSP F16 satellite launched on 18 October 2003. The digisonde ground-based electron density profiles serve as "ground truth" for the satellite-borne UV optical measurements of "F layer" and "auroral E layer" electron densities. Data storage and processing capabilities were developed to handle the large number of data sources and time intervals for fly over events. Real data requests, measurements, manual data editing, and reports were successfully handled.

## 1.8 Autoscaling Refinements

The quality of the ARTIST autoscaling continued to be of concern since the introduction of the ARTIST 4.0 version 0702 in early 2003. By the middle of 2004, the total number of implemented improvements became significant enough to release a new version,

ARTIST 4.5. The deficiencies in the previous product and the improvements offered by ARTIST 4.5 are discussed.

## 2    COPEX - EQUATORIAL SCINTILLATION

### 2.1    Introduction

Following the analysis of the COPEX campaign data presented in the previous annual report, attention was turned towards the details of the early stages in the development of ionospheric (F-region) instabilities that precede the growth of equatorial bubbles. For this investigation, ionograms from Jicamarca, Peru, Cachimbo and Sao Luis, Brazil were examined over two time periods to determine which days were quiet (no satellite traces on the ionograms, no spread F and no bubbles) and which days were active. The time intervals used here were first the COPEX campaign (1 October through 9 December 2002) and then the sixty-day period from March through April 2003. The second period was chosen because during that time the solar declination was the conjugate of the solar declination during the COPEX campaign period.

### 2.2    Satellite Trace

In order to better understand the character of the earliest F-layer deformations that appear as "satellite" traces in ionograms on active nights, a simulation program was developed using the raytracing code by Xueqin Huang [Reinisch et al., 2005]. These satellite traces usually appear shortly after the vertical velocity maximum associated with the pre-reversal enhancement. An example of these traces is shown in Figure 1.
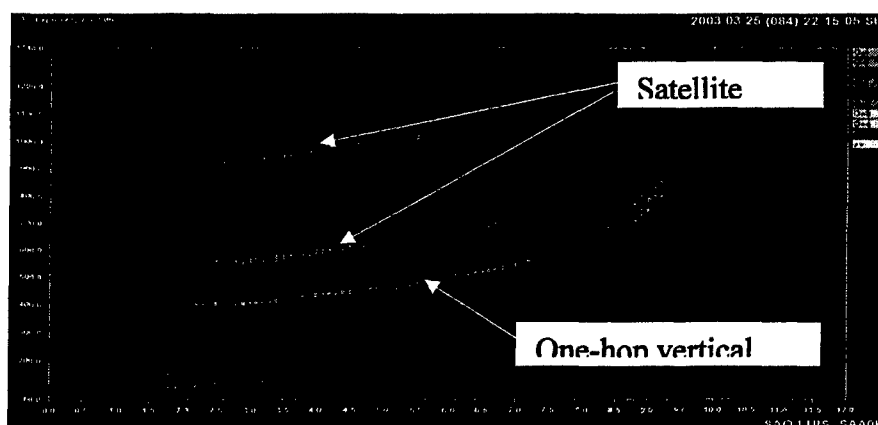


Figure 1. Typical Appearance of "Satellite" Traces as the Earliest Indicator of F-layer Instability Growth. Sao Luis, Brazil on 25 March 2003, 2215 UT.

A simplified electron density model of the early stage deformation of the bottomside F-layer was developed that could be modified in terms of the altitude, width, depletion ratio, steepness of the walls, and location relative to the sounder. A typical example used with the ray-tracing program is shown in Figure 2.



P
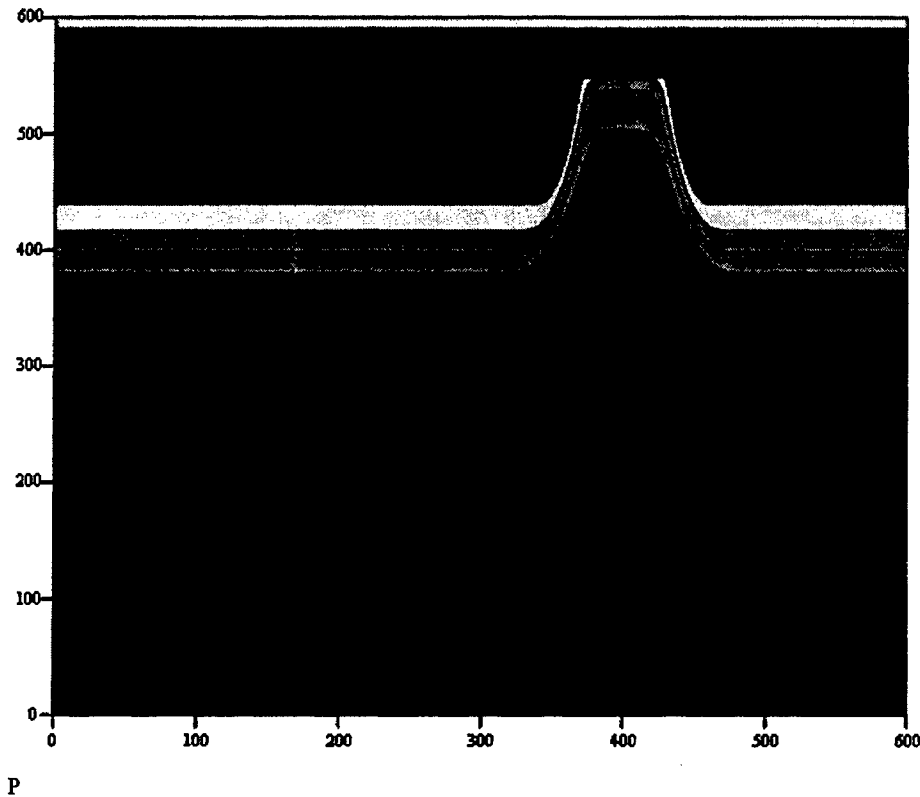
**Figure 2. Early Bubble Model Set in a Background Ionosphere at a Distance of 400 km From the Sounder**

Here, the background F-layer model used had a peak height of 500 km and a critical frequency of 6.0 MHz. The proto-bubble shown in the figure had a width of 100 km and was located 400 km from the sounder. This model is assumed to extend uniformly in the direction perpendicular to the page. The ray tracing was done at 0.5 MHz steps starting at 3 MHz.

The example of the rays superimposed on the model is shown in Figure 3. Here, the bubble was located at 200 km from the sounder location and the ray tracing was done at 3 MHz. Although the majority of the rays, launched every 1°, reflect from the bottom of

the layer, there is a small bundle of rays (denoted in the figure as back-reflected) that returns to the sounder. These back-reflected rays originate near where the rays are orthogonal to the plasma frequency contours. A program was developed that searches automatically for these back-reflected rays and the results, as a function of frequency, are shown in Figure 4 as simulated ionograms. The vertical trace was calculated by using vertical take-off angles and the background F-region profile.
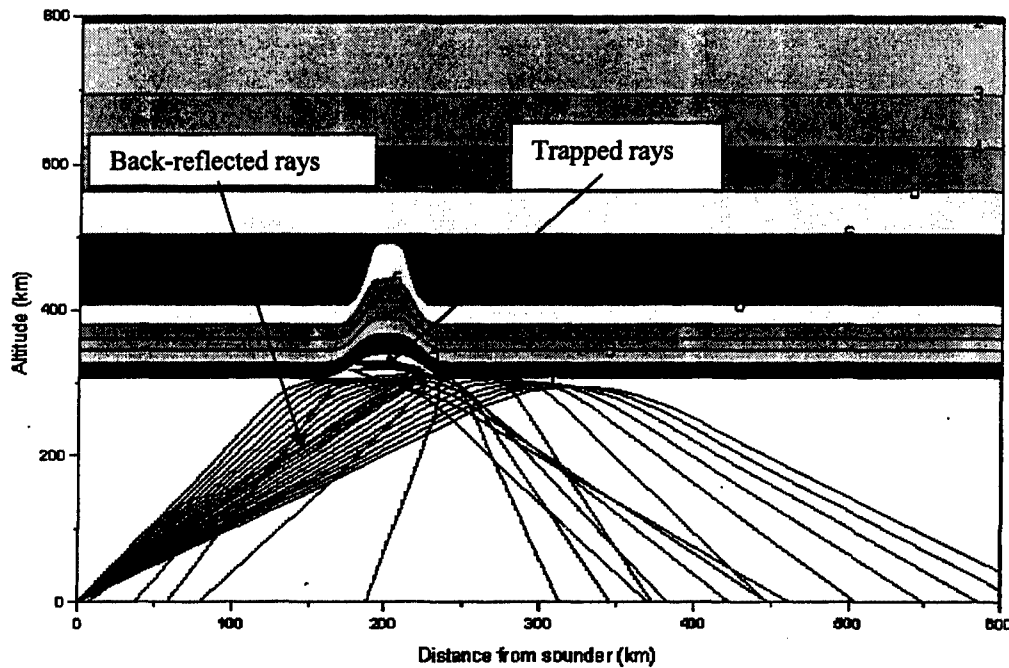


**Figure 3. Bubble Modified Profile with 3 MHz Rays Superimposed**

6
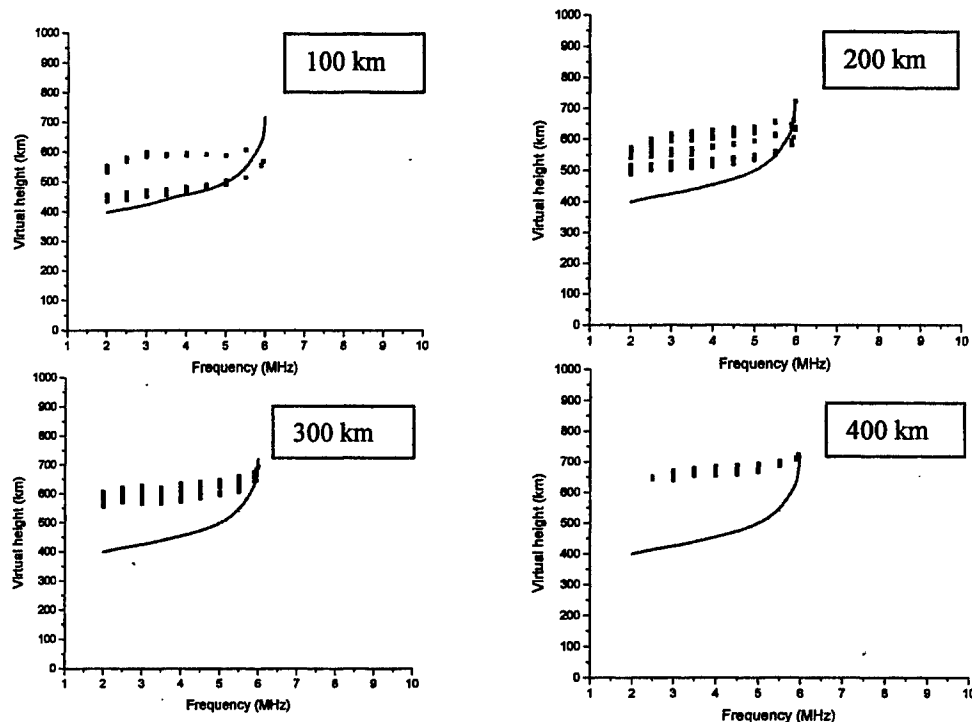
**Figure 4. Simulated Ionograms with Bubble Distances of 100, 200, 300 and 400 km From the Sounder as Labeled. The Range Extended Satellite Traces Result from the Spread in the Time Delay Associated with the Back-reflected Signals.**

These simulated satellite traces can be compared with the actual ionograms and used to determine the ranges to the bubbles. For fully developed bubbles (i.e., beyond the early phases that generate the satellite traces) an extension of the bubble trace beyond the F-layer critical frequency is often observed (see Figure 5). It has been hypothesized [Sales et al., 1996] that these signals originate by relatively strong backscatter from decameter scale field-aligned irregularities embedded within the walls of the bubble. For the example shown in Figure 5, the F-layer critical frequency was approximately 9.3 MHz, while the bubble trace extension was observed out to 13.5 MHz with decreasing amplitude as the frequency increases away from the critical frequency. Irregularities in the F-region near the peak of the layer may be able to scatter waves with frequencies greater than foF2. The potential for observing this type of backscatter is indicated by the trapped rays within the bubble structure as shown in Figure 3. Any ray reflecting from the walls of the bubble can be returned to the sounder along the same path since orthogonality with the local magnetic field is assured for equatorial geometry. The effect of such backscatter rays was not included in the synthesized ionograms shown in Figure 4. Further investigation into this area is required.

7
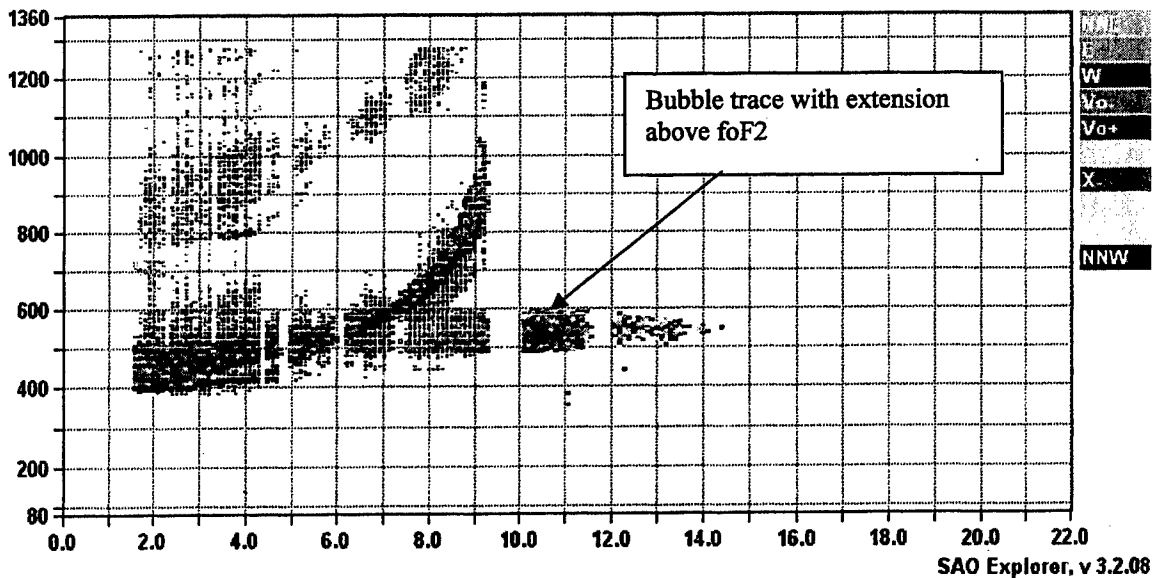
**Figure 5. Jicamarca Ionogram Showing a Scattered Signal Trace from a Bubble as it Approaches the Overhead Position. The Frequency Gaps in the Trace Result from Protected Frequency Bands at Which the Sounder is not Allowed to Transmit.**

**Quiet Days**

The number of observed quiet days (days when no satellite traces appear, no bottomside spread F or bubbles was generated) at the three sounders located across South America was very different. These are shown in Figures 6 (COPEX) and Figure 7 (March-April 2003). For The March-April data set (Figure 7) an additional category was introduced, i.e., counting days when no bubbles appeared although there were satellite traces and possibly some bottomside spread F.
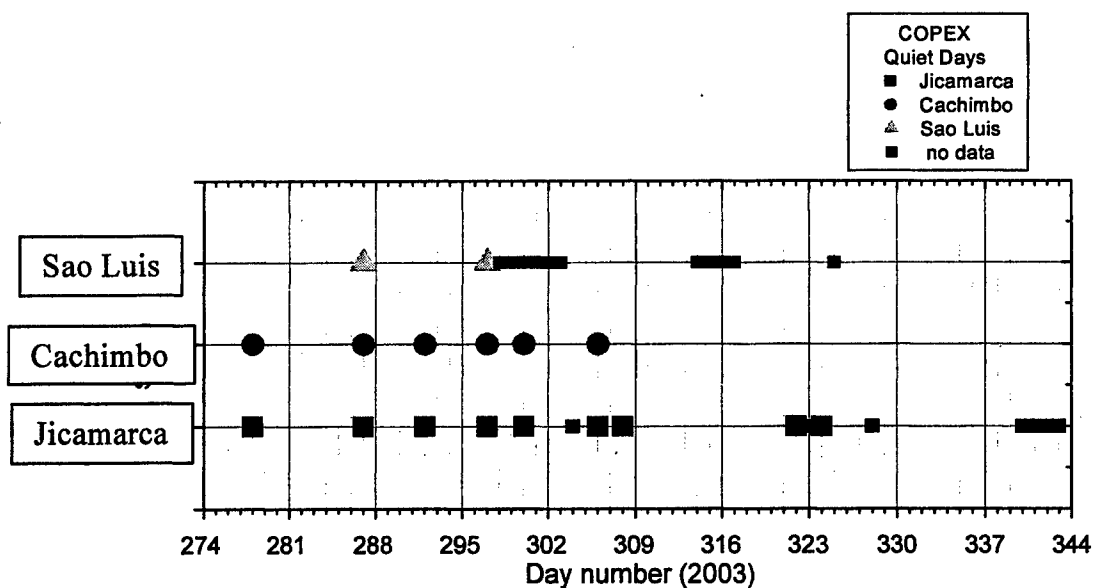
**Figure 6. Distribution of Quiet Days During COPEX at the Three Sounder Locations.**

Two characteristics become apparent after examining both sets of data. First, there are more quiet days as one moves from east to west and secondly, there are more quiet days during the March-April period than the October-December period (COPEX). This second observation may not be surprising, as the data interval lies closer to the May through September period when scintillation activity reaches a minimum. From the March-April data set the number of quiet days increases as the end of the period approaches. For COPEX, the number decreases in late November and early December as we move further away from the May-September scintillation quiet period.
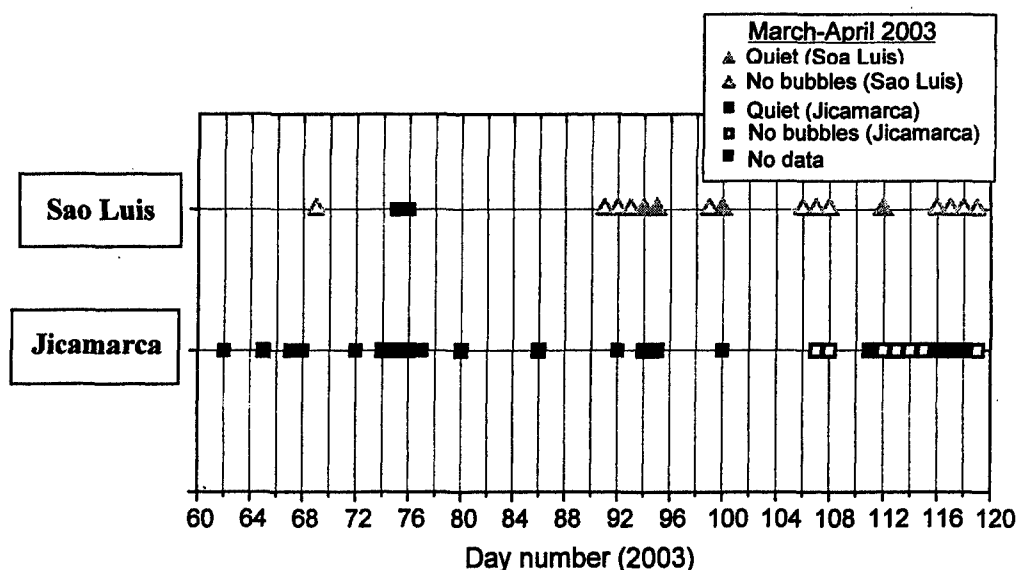
**Figure 7. Distribution of Quiet Days During the March-April 2003 Period.**

An additional category was added to this analysis for the March-April 2003 time interval. Here days were included as quiet when, although some satellite traces were detected, no bubbles were observed in the vicinity of the particular station. A more detailed review of these data is necessary to understand the relationship between the occurrence of quiet days on the east and west coasts of South America. It is planned to continue this investigation in the next year.

## 2.3 Vertical Drift Velocity and Instability Development

Using the data collected during digisonde "drift" mode measurements made it possible to investigate the relationship between layer height and upward motion and the development of Raleigh-Taylor (R-T) instabilities. The Jicamarca data from both the COPEX and the March-April 2003 period (Figure 8) provides the best comparison.

10
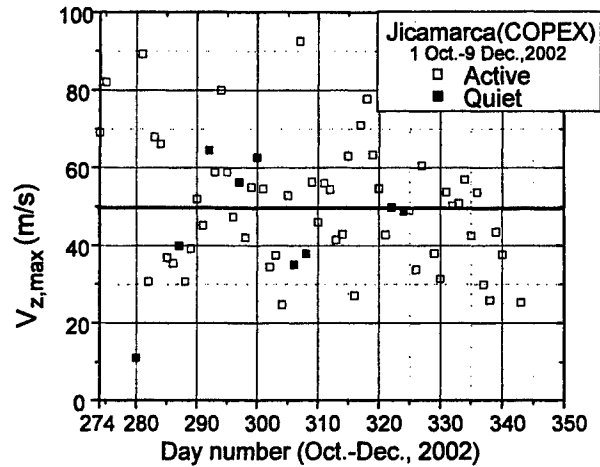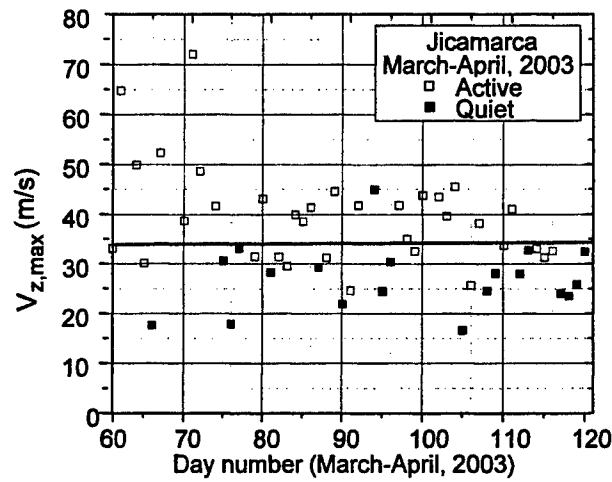
**Figure 8. Maximum Pre-reversal Vertical Drift Velocity Measured at Jicamarca During October-December 2002 (a) and March-April 2003 (b). The Horizontal Lines Represent the Median Maximum Velocity for Each Period.**

The median maximum velocity decreased significantly from the October-December period to the March-April period. In October-December the median velocity was 49 m/s compared to 37 m/s in March-April. This corresponds to the significant increase in the number of quiet days going from 13% during October-December (COPEX) to 36% during the March-April period including both the quiet and the no bubble days. Counting only the quiet days the probability of a quiet day still increased to 23%, almost double the probability during COPEX.

This emphasis on the maximum pre-reversal vertical velocity is based on the observation that the formation of satellite traces appears to occur very closely to the

maximum upward motion. For example see Figure 9, where the plasma frequency contours from the ionogram inversion program show the rapid rise at the maximum $V_z$ and the onset (vertical dotted line) of the satellite traces on 11 October 2002.



**Contours, JI91J, DPS-1, SAO Explorer, v 3.2.08**
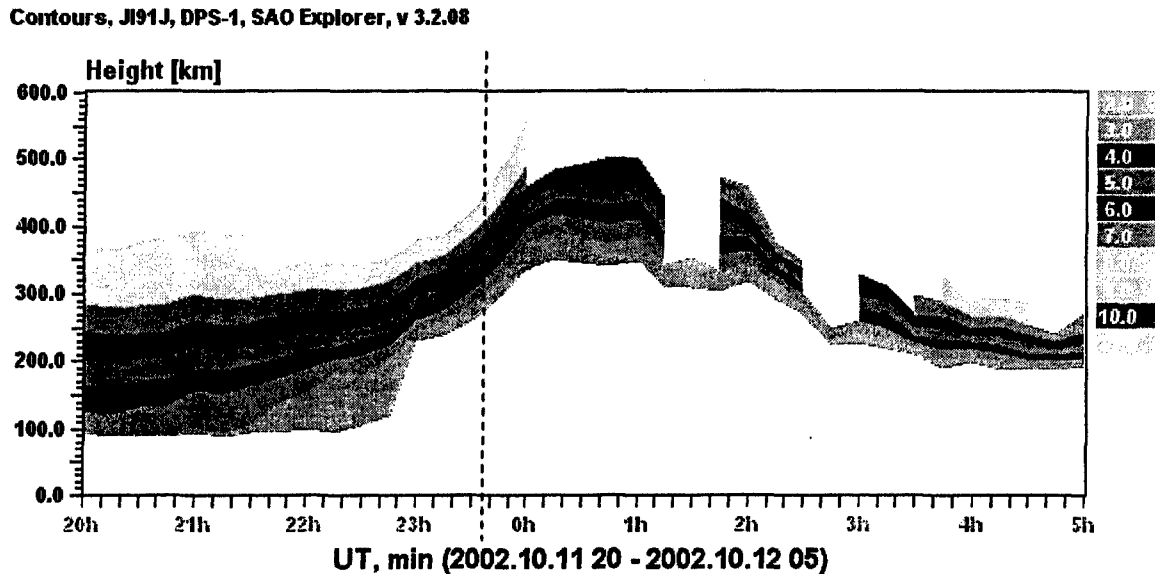
Figure 9. The Plasma Frequency Contours for 11 October 2002 from 20 UT to 05 UT. The Vertical Dotted Line Denotes the Time of Satellite Trace Onset, Coincident with the Maximum Upward Layer Motion.

The hypothesis presented here is that quiet days are significantly more likely when $V_{z,max}$ is small, i.e., $V_{z,max} \leq V_{z,median}$. The statistics from Jicamarca certainly lean in this direction. For the March-April period, the probability rises dramatically when $V_{max}$ is less than the median vertical velocity. Of the nineteen observed quiet days in this period, only one day had $V_z$ greater than the median velocity. For the COPEX campaign the situation was not quite as clear. Here, of the nine observed quiet days, three days had $V_z$ greater than the median vertical velocity.

Clearly, there is a direct relationship between the vertical velocity and the height of the F-layer. The basic theory for the initiation of the R-T instability indicates that the greater the height of the layer, the greater the instability growth factor becomes. The actual height of the bottom of the layer depends on the initial height before the layer begins to move upward. Future efforts must be directed towards establishing a relationship

12

between the maximum vertical velocity and formation of these instabilities. This investigation will focus on the time difference between the time of maximum $V_z$ and the onset of the satellite traces. The speed of the upward motion may be as important as the actual height of the layer at the onset time. In last year's effort on this subject it was established, using the COPEX data set, that the height of the layer alone was not a good indicator of bubble formation. Therefore the investigation will pursue a combination of layer height and layer speed as the controlling factor.

## 3    VLF TRANSMISSION OBSERVATIONS WITH IMAGE/RPI

In the frame of the present project we continued our work on ground VLF station monitoring with the RPI/IMAGE instrument. Using the passive, so-called "dynamic spectrogram" mode of the RPI instrument we have been able to successfully identify transmissions from ground-based VLF stations using the retrospective analysis of our 2001-2002 observations. These results have been presented in our last annual report. However, since the original RPI instrument settings used in those measurements were aimed at receiving relatively weak noise signals, the system gain settings were not optimal for reception of the strong signals associated with the VLF transmissions from the ground. Therefore, most of the time when receiving VLF transmissions the RPI receiver was saturated, making it impossible to perform statistical quantitative analysis of the large amount of available data. To avoid this problem a dedicated operational mode with lower receiver gains was designed and implemented.

### 3.1    System gain calibration

Accurate receiver calibration has always been an issue in the past. Unfortunately, the relatively small available amount of measurements made with different system gain settings did not allow us to unambiguously resolve this problem. For the latest experiment we have accumulated about 2 months of data representing over 10,000 individual observations. During September and October 2003 we ran a series of sequential measurements with the system gain settings G1 (base gain), G2, G3, and G4, and then during the summer of 2004 another round of measurements where a pair of settings G1 and G15 was used. G15 was the standard gain setting for all the previous data

collected. Statistical analysis of the large data volume allowed us to measure relative system gains used in RPI instrument operational modes. Our first attempts involved visual comparisons and fitting with log-normal distributions, but the results were not very convincing, and we undertook another effort. The new approach was to compare the measured signal strengths at several gain settings using only data where there was a close coincidence in time between several gains. The amplitude of each data set was adjusted to minimize the RMS difference between itself and the G1 measurement. The results are presented in Table 1.

Table 1. Relative Gain Settings Deduced from the Measurements

| Gain setting | Documented gain, dB | Measured gain, dB |
|---|---|---|
| "G1" | 0 | 0 |
| "G2" | 6 | 2 |
| "G3" | 12 | 8 |
| "G4" | 18 | 27 |
| "G15" | 36 | 37 |

Internal noise at the lower gain settings and saturation at the higher gain setting limit the goodness of the fitting process although these results appear to be considerably more reliable.

This new knowledge about the gain ratios and received signal amplitude distribution not only helped us to select the optimal program for future VLF signal reception, but also allowed us to better understand other results obtained with the RPI instrument in its active sounding mode.


### 3.2 VLF Station Monitoring in Space

RPI observations dedicated to VLF station monitoring were routinely run in the period from 1 September to 23 November 2003. This program was in operation when the satellite was in the vicinity of perigee. Figure 10 below shows a typical IMAGE satellite orbit configuration in the solar-magnetic coordinate system during this period of time. It is clear that during its closest approach to the Earth the satellite is located in the Earth's shadow.
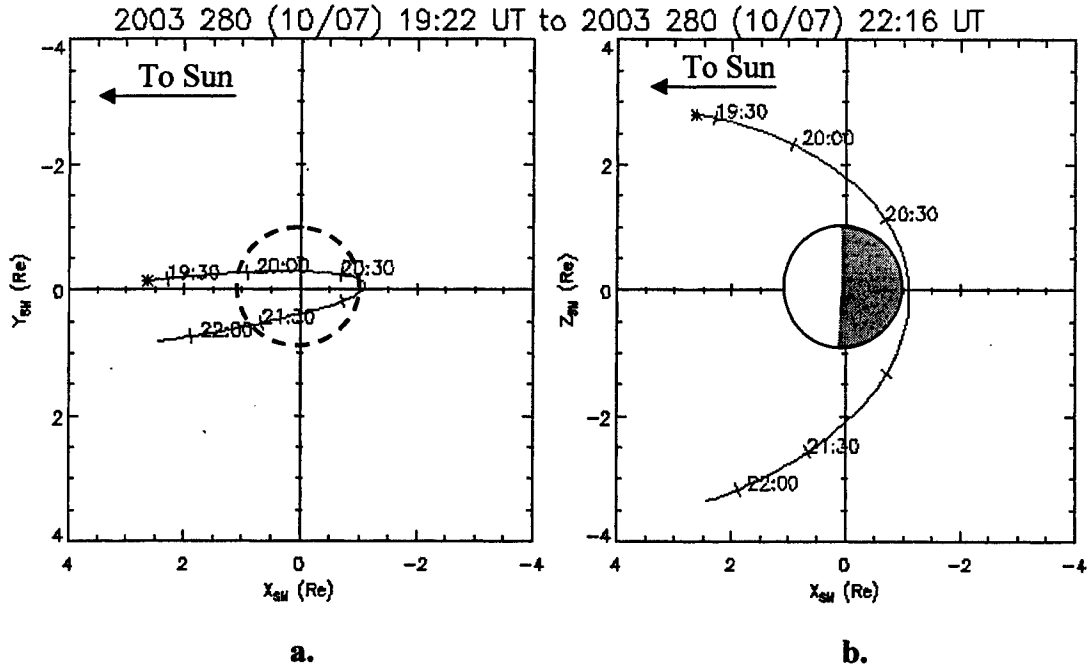
**Figure 10. Typical IMAGE Orbit Configuration for Year 2003 Observations. In the Solar-magnetic (SM) System of Coordinates the X-axis Points Towards the Sun, and Z-axis Points Towards Earth's North T Magnetic Pole. Thus, Panel (a) Shows a "Top" View, while Panel (b) Shows a Corresponding "Side" View.**

Thus, a majority of the VLF station observations in 2003 were made during nighttime conditions. Another series of experiments was carried out in the summer of 2004. During this time the IMAGE orbit was not optimally positioned for the VLF signal reception, however, and therefore, these measurements provided a significantly smaller amount of new data.

A generally accepted model of the VLF signal propagation consists of three different propagation stages. At the first stage the VLF signal emitted by the transmitter propagates in the earth-ionosphere wave guide. Primarily in the vicinity of the station a certain amount of signal energy leaks through the ionosphere into the plasmasphere. Clearly, since the signal frequency is very low, such a wave can only propagate in the whistler mode meaning that from the ionosphere the signal propagates essentially along the magnetic field line. Little is known about the specifics of this leakage mechanism as there have not been many dedicated experiments to understand how much signal propagates

15

through the ionosphere. Our goal is to confirm this propagation model and to study the main characteristics of this process.

Qualitatively, the overall picture from our 2003 and 2004 observations was similar to our previous results. As, before, the station signal was detected when the satellite was inside Earth's plasmasphere. Three stations were selected for the analysis: NML, NLK, DHO. Three other stations used in our earlier observations were excluded for the following reasons: the NAA station was not operating during the period of these measurements, the NWC signal was contaminated with strong interference, and the NPM station location was not well covered by the satellite because of the orbit configuration.
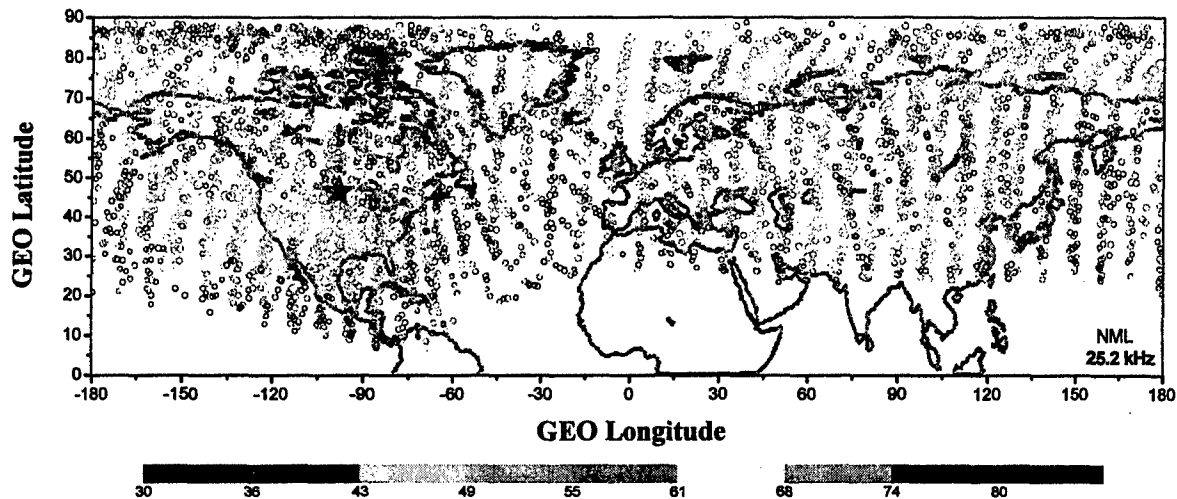


**Figure 11. Observations of the NML Station Made in 2003. The Position of Each Circle Corresponds to the Location of the Magnetic Footprint of the IMAGE Satellite Shown in Geographic Coordinates. The Black Star Indicates the Location of NML.**

Figure 11 presents a summary of the received signal from the NML transmitter at 46.4° north, 261.7° east during this period. The amplitude of the detected signal is indicated by the size of the circle. Amplitude values here are presented in terms of raw digitizer units (dB). The position of each circle corresponds to the location of the magnetic footprint of the IMAGE satellite in geographic coordinates. It is evident that the signals from the ground-based VLF station are readily detected with the RPI instrument. Figure 12

16

presents the signal amplitude as a function of the distance between the station and the satellite footprint, calculated for the DHO station in Germany. We estimate the area "highlighted" by the ground VLF transmitter to be of the order of ~2000 km in radius (beyond this distance the received signal strength decreases by 20 dB). This results in the overall signal decay of the order of 10 dB / 1000 km, which is approximately the same value found for the other two stations for nighttime conditions.
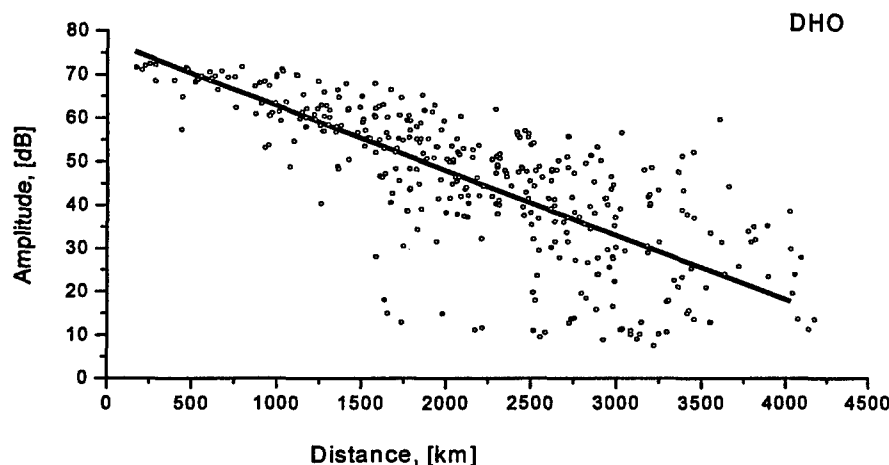


**Figure 12. Signal Amplitude as a Function of the Distance Between the Station and the Satellite Footprint, Calculated for the DHO Signals. Black Circles Show Individual Measurements, and the Thick Curve is an Average Signal Decay.**

It should be noted that the observed signal amplitude decay in Figure 12 is associated with the first stage of the propagation, namely, with the signal propagation in the earth-ionosphere wave guide. This conclusion is supported by the fact the observed "highlighted" area around the station is almost an order of magnitude smaller during daytime observations. This effect was clearly demonstrated in our 2001-2002 observations and is confirmed in the 2004 measurements. Such "confinement" of the signal around the station also supports the fact that the signals indeed propagate in a small cone along the magnetic field lines where the wave leaked through the ionosphere. Unfortunately, the small amount of daytime observations made in 2004 (in 2003 there were essentially no daytime measurements) does not make it possible to deduce a numerical value for the daytime rate of the signal decrease, but visually it is estimated to be significantly higher than the nighttime value (approximately 30 dB / 1000 km).

17

An interesting effect was observed when the signals are divided according to satellite position. Figure 13 presents the same NML data with the satellite footprints limited to the vicinity of the station. This plot is presented in geomagnetic coordinates. The left panel shows the observations made when the satellite itself was located in the northern hemisphere, while the right panel presents the measurements made when the IMAGE satellite was in the southern hemisphere. It is evident that for the northern hemisphere observations the strongest signals were observed during the closest approach of the footprint to the station location. However, for the observations in the southern hemisphere the maximal signals appear to be offset towards the lower magnetic latitudes. This effect was investigated more thoroughly.
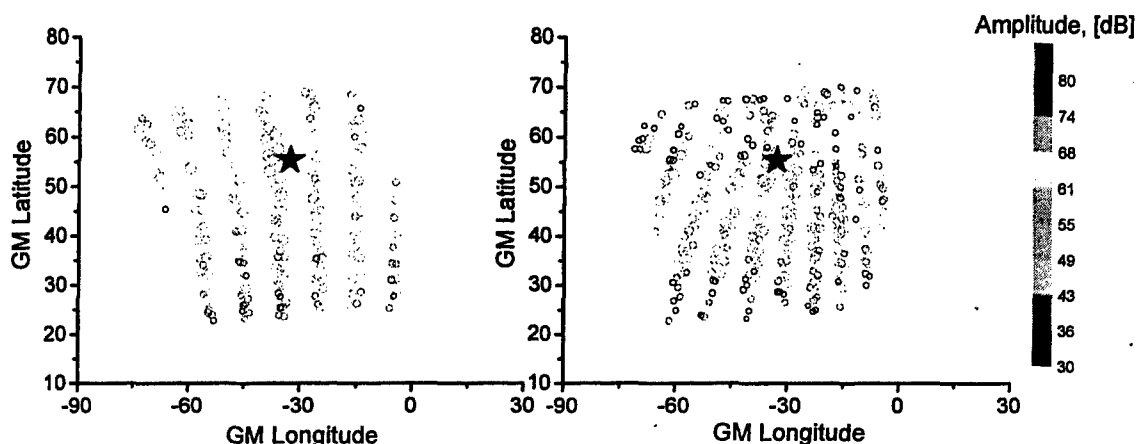


**Figure 13. Observations of the NML Station Made from Northern (Left Panel) and Southern (Right Panel) Hemispheres. Satellite Footprints are Shown in Geomagnetic Coordinates.**

Figure 14 is a composite plot presenting detected signal amplitude as a function of the satellite position in geomagnetic coordinates. Scattered circles show the received signal amplitudes, with the continuous black curve as the best fit smoothed median amplitude. The figure also shows the magneto ionic Y-parameter (ratio of the gyro frequency and signal frequency, $f_{ce}/f$) calculated at the equator for the L-shell corresponding to the satellite position. Regions where the magnetic footprint of the satellite falls in the close

18

vicinity of the station (a box of 5° in geomagnetic latitude and 30° in geomagnetic longitude) are shown as the shaded columns. This plot, in fact, shows the same offset effect in greater detail, demonstrating the displacement of the strongest signals in the southern hemisphere towards the lower latitudes. It also confirms that the VLF signal indeed propagates to the satellite in the opposite hemisphere through the plasmasphere, not via the earth-ionosphere waveguide. If this were not true, strong signals would be detected in the equatorial region, which is clearly not the case.
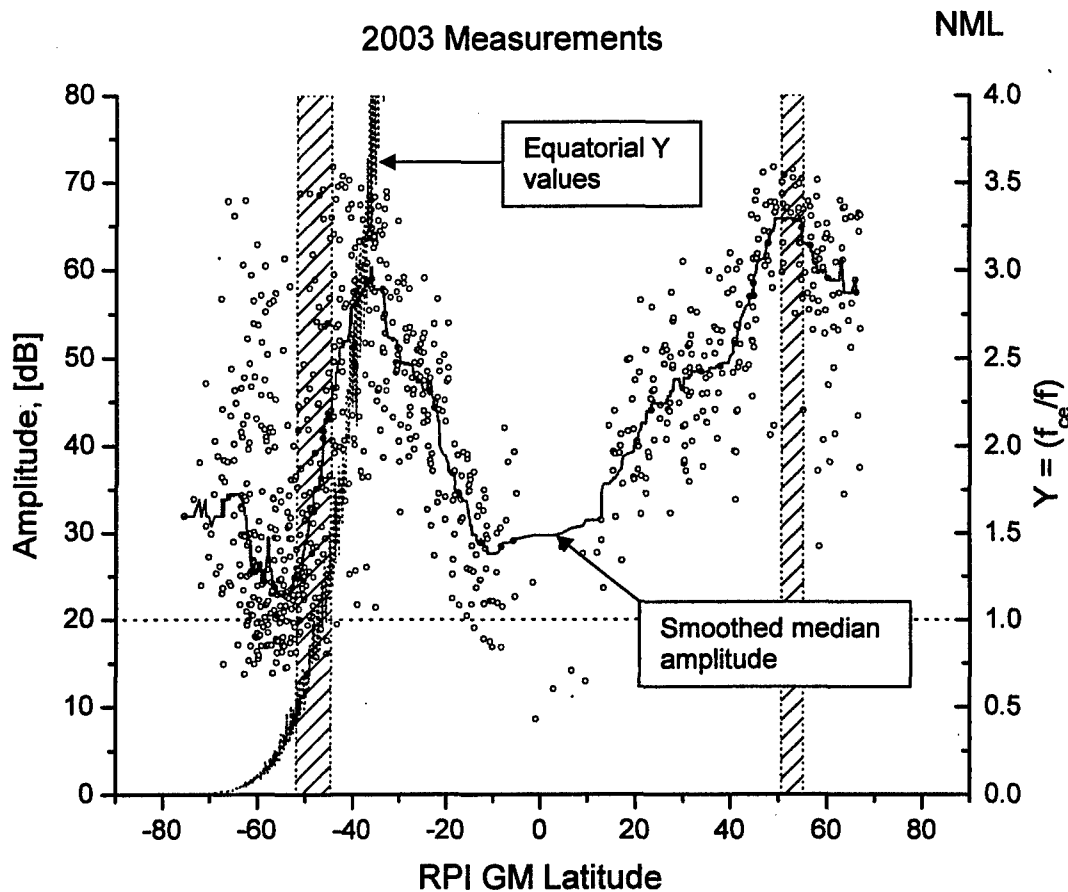
Figure 14. Signal Amplitude as a Function of the IMAGE Satellite Position. Circles Represent Individual Measurements.

The calculated Y value provides an explanation of the strong signal displacement observed in the southern hemisphere. By definition, whistler waves can exist only when

the wave frequency is lower than the gyro frequency (*i.e.*, Y > 1). The signal originating from the ground station on its way along the field line from the northern to the southern hemisphere goes through the equatorial region with the weakest magnetic field, and therefore, lowest gyro frequency. It is quite possible, that under certain conditions, at the equator the wave frequency becomes equal to or even greater than the local gyro frequency, as illustrated by Figure 14 (regions for which corresponding equatorial value of Y is smaller than unity). Clearly, for the satellite positions at about 30° magnetic latitude (this is also the location where the satellite magnetic footprint is in the closest vicinity of the NML station, and therefore, the strongest signal is expected) the corresponding equatorial Y value is near unity and, therefore, the signal cannot propagate across the equator. This explains why the NML signals are not observed at this satellite position. When the satellite is at the lowest geomagnetic latitudes, the corresponding equatorial Y-values are significantly larger (see Figure 14) allowing for the signal penetration into the southern hemisphere. This results in an apparent "offset" of the region associated with the strongest signal amplitude towards lower latitudes.

The signal "migration" is not observed for the DHO signals, but was detected for the NLK signals, in good agreement with the gyro frequency values calculated for the corresponding magnetic tubes. The observations of the VLF signals from these two stations (both located in the northern hemisphere), made during 2003 and 2004 are consistent with the suggested propagation mechanism.

We have also made another effort to estimate the absolute value for the VLF signal strength. The main difficulty here is that the effective antenna length, translating field strength into the receiver input voltage, is not exactly known. Nevertheless, with the current absolute calibration being used, our measurements show that the peak VLF signal amplitude is of the order of 200 $\mu$V/m, corresponding to a Poynting flux of about $2.6 \times 10^{-10}$ W/m$^2$ for a flux-tube of 2000 km radius. This would mean that less than 1% of the total power radiated by the ground-based VLF station is transmitted through Earth's ionosphere into the magnetosphere.

# 4 VLF INDUCED ELECTRON PICTH ANGLE SCATTERING (IEPAS)

The objective of this investigation is to use manmade Very-Low Frequency (VLF) waves to stimulate the wave-particle interaction in the radiation belt. The results of the enhanced interaction, if successful, would substantially reduce the lifetime of the relativistic electrons in the belt by pitch-angle diffusion of the particles into the atmosphere. In the past year, several studies were carried out and many of them remain active. They include the concept study of the Low-earth Orbit Relativistic Electron Remediation System (LORERS), planning studies for a transmitter on Cygnus, a trade-off study of a capacitance-loaded antenna, operation and data analyses of RPI monitoring ground-based VLF transmitters, and RPI experiments of whistler wave transmission. All these studies provide significant knowledge for the feasibility of the IEPAS concept. In the following we summarize our results in terms of scientific issues because the physical understanding can be applied to different mission scenarios by using corresponding parameters.

There are five scientific issues: (a) VLF wave radiation, which studies the wave propagation in plasma from a given source of radiation; (b) Processes in the plasma sheath, a region of net electric charges near the antenna when the transmitter is charged to a high voltage; (c) Space-borne VLF transmission experiments, which provide baseline knowledge about the space whistler transmission and plasma sheath; (d) Transmitter conceptual designs which integrate knowledge that is learned in the first three studies; and (e) RPI monitoring of ground-based VLF transmissions, which is used to understand the efficiency of ground-based VLF wave penetration of the ionosphere into the magnetosphere. The VLF monitoring area was reported above in section 3.

Based on the results we have derived, it is likely that a ground-based system may not be feasible because only a few percent of the wave energy couples through the ionosphere. The ground-based transmission monitoring study also indicates that the raytracing codes widely used in the field may not describe reality. This has implications to understanding space-borne VLF-wave generation method. In the space-borne VLF transmitter design, our analyses show that the plasma sheath will be the ultimate limit of radiated power

even if the tuning issue, which will be discussed below, is resolved. To reduce the sheath effects and increase the radiated power, the transmitters should be located in regions of higher plasma density and stronger magnetic field and should operate at the highest possible frequencies. This is in favor of a lower orbit, such as LORERS. However, with this lower orbit the wave-particle interaction time is expected to be shorter because of the greater spatial changes in the density and field strength. Furthermore, how long the waves can be trapped in a flux tube with adequate amplitudes during propagation become important in the overall assessment. In other words, it becomes essential to correctly model the waves, for example using raytracing codes, from the transmitter propagating in the magnetosphere. The orbit of a most effective system will depend on the quantitative evaluation of all these factors.



Dipole antenna with plasma sheaths                    Equivalent circuit
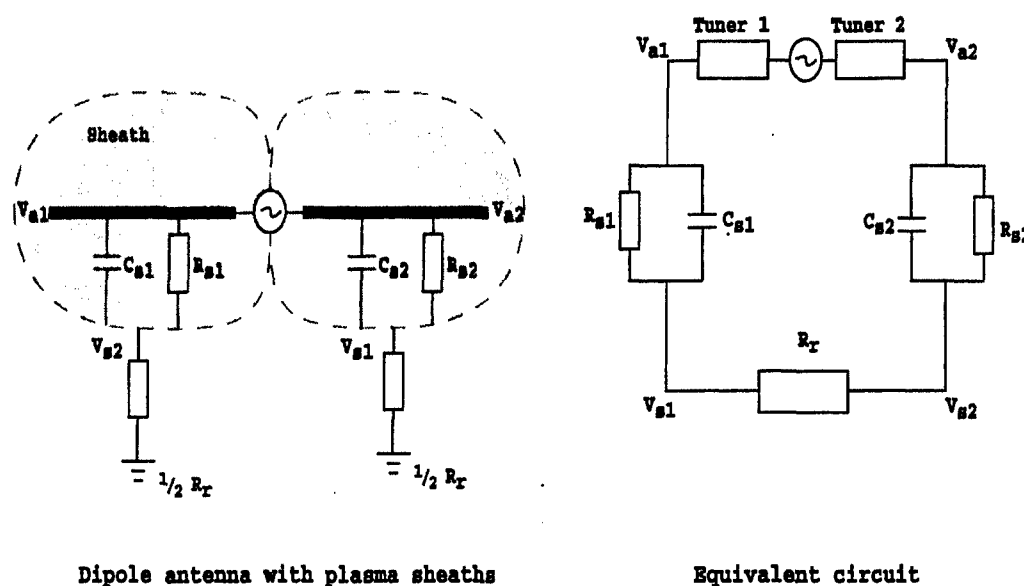
Figure 15. Equivalent Circuit of the Transmitter-antenna-sheath-plasma System. Rr is the Radiation resistance, Cs and Rs are Sheath Capacitance and Resistance, and Va and Vs are Voltages at the Antenna and at the Boundary Between Sheath and Plasma. Note that Only the Circuit Current and Va, as well as the Voltage at the Transmitter Source (Before Tuner) may be Measured.

## 4.1    VLF Wave Radiation

This is a theoretical investigation of how whistler waves propagate from a source of current in regions farther than a few kilometers from the satellite. This theory considers

22

waves radiated from the antenna in all directions for a finite-length antenna in contrast to an infinitely short antenna [Belmain, 1964]. The source of the waves is a current which, when integrated with the knowledge learned in the plasma sheath study, is located at the boundary between the plasma sheath and plasma proper, instead of the antenna surface. The analytical portion of the study is nearly completed and we are still working on the numerical portion. The results of this analysis are to provide the relationship between the driving antenna current and the wave amplitudes in the far field. As we will see below, the current is a key physical quantity in the transmitter system design and it also determines the properties of the plasma sheath. From our analysis, the radiated wave amplitudes along the field line are

$$\mathbf{E} \propto I_a \cdot f_{pe}^1 \cdot f^{1/2} \cdot f_{ce}^{1/2} \cdot r^{-1/2}$$
$$\delta\mathbf{B} \propto I_a \cdot f_{pe}^2 \cdot f^{1/2} \cdot f_{ce}^{-1/2} \cdot r^{-1/2} \tag{1}$$

The most important information gained above is that to increase the amplitudes of the waves, the transmitter should be placed in regions of high plasma density and operated at high frequencies. This is because even for the same Poynting flux, the magnetic component of the wave, which is most important for IEPAS, can be different. The amplitudes decrease with the distance along the field as $r^{-1/2}$. In the directions transverse to the field, they drop with the same rate as $\rho^{-1/2}$ where $\rho$ is the distance from the field line that intersects the satellite. Therefore, the region of the space covered by the waves has a shape between a conic and a column. The effective region of the wave should be defined as the region with amplitudes greater than a certain value, say, large enough to produce enough pitch angle scattering. Then the cross-section of the flux tube can be determined for the purpose of assessing the effectiveness of an IEPAS system.

### 4.2    Plasma Sheath

For space-borne transmission, different from vacuum conditions, the antenna is submerged in the surrounding plasma, which is composed of ions and electrons, and electrically highly conducting. When the antenna transmits, the two branches of the dipole antenna are charged with equal but opposite voltages, forming an electric field surrounding the antenna. The charged particles in the plasma move in opposite directions under such an electric field; the electrons are attracted to the positively charged branch of

the antenna and the ions to the negatively charged branch. The currents created by these motions tend to cancel out the antenna driving current. Furthermore, the transmission current, which flows along the antenna, generates a magnetic field, which in turn affects the motion of the charged particles. The particle response time to the electromagnetic field generated by the transmission is determined by their characteristic periods; gyro motion and oscillation. The whistler mode frequency in the region for a space-borne IEPAS system is between the electron gyro frequency and the ion plasma frequency. Under such a rapidly changing electromagnetic field, the electrons, because of their smaller mass, will respond quickly enough to move back and forth with the driving field from one branch to the other while the ions will essentially stay still. This particular situation causes a unique phenomenon: formation of the plasma sheath, which is a region near the antenna where excessive charged particles of one type occur. The quasi-neutrality approximation used in plasma theory is no longer valid. The sheath functions as a shield to prevent the electromagnetic field from being transmitted. Understanding quantitatively the sheath processes and the controlling factors is crucial to designing a space transmitter.

We have investigated the sheath problem with a first-principles approach, starting from the basic equations. The physical processes in the sheath are now understood in theory, see Figure 16. Because the current diminishes at the antenna tips, due to charge conservation, electric charges occur on the surface of antenna. The charge density has a 90° phase shift from the current and is nearly in phase with the antenna voltage. The thickness of the sheath varies with antenna voltage/surface charge during a wave cycle. If the antenna is insulated, no current flows into the sheath. An ion or electron sheath forms on each side of the antenna according to the antenna voltage. When the voltage varies with time, a current occurs as the sheath-plasma boundary moves. At the sheath/plasma boundary, the voltage is non-zero because of radiation.

Radiation
Current

Plasma

Boundary
Motion

Ion Sheath

Antenna

$r_s$

$V_s$

$r_a$

Plasma

Boundary
Motion

Ele Sheath

$V_a$

Antenna

Driving
Current
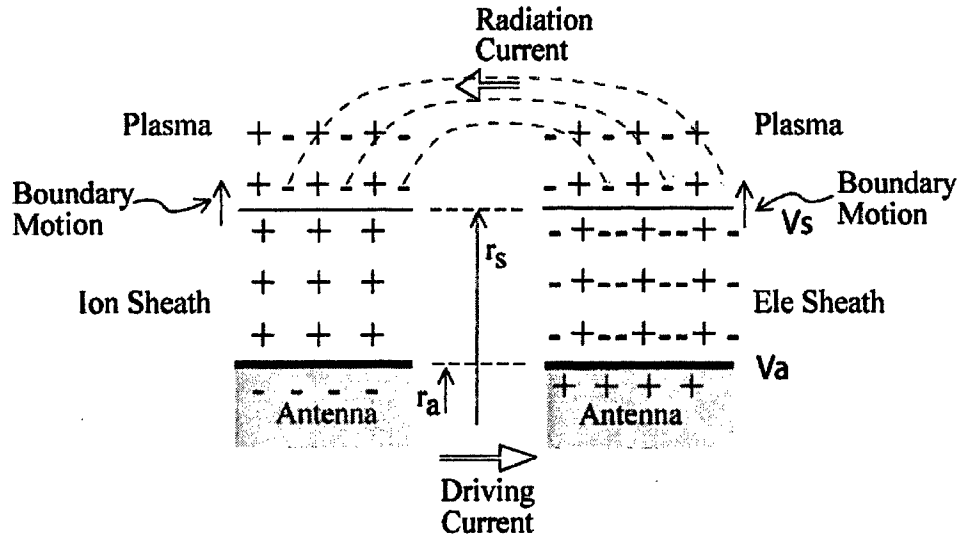
**Figure 16. Physical Processes in the Plasma Sheath Surrounding an Antenna. The Dashed Lines with Arrowheads Indicate the Electron Motion in the Next Moment as the Boundaries Between the Plasma and Sheath Move up.**

A most important gain in our knowledge from this investigation is the understanding of the antenna charging process. If the antenna is not insulated, in the processes described above, electrons will hit the antenna surface that is positively charged. If there is no significant photoelectron emission, after a few wave cycles, the antenna is charged to a negative DC voltage, which is close to the amplitude of the antenna driving voltage. Under this situation, when the driving voltage is zero, the antenna is negatively charged with an ion sheath on both sides. When the driving voltage is not zero, one side of the sheath shrinks and the other side thickens.

This raises one of the most important questions in transmitter designs: should the antenna be bare or insulated? For an insulated antenna, the antenna will not be charged. However, the antenna will be hit constantly by high speed electrons, which are accelerated to a few keV in energy. The kinetic energy of the particles will be converted to thermal energy when they are stopped at the surface of the insulation layer. In other words, much of the transmitter power is used to heat the antenna. The insulation of the antenna may not be able to last a long period of time.

For a bare antenna system, on the other hand, a dynamic process of charging may occur in a few wave cycles. The antenna voltage is the summation of charge voltage and the driving voltage. After the antenna is charged negatively to the amplitude of the driving voltage in the dynamic process, the antenna voltage will remain negative during a wave cycle and the electrons will not be accelerated as they approach the antenna. Heating of the antenna will occur only in the dynamic process. After that, there is little leaking current through the sheath and tuning may be easier to manage.

The sheath reactance for a cylindrical antenna is

$$|X_s| \approx \frac{\ln(r_s/r_a)}{\omega 2\pi\varepsilon_0 l}$$

$$\text{where } r_s^2 = r_a^2 + \frac{I_{a0}}{\pi e N_0 \omega l}$$

(2)

For a space antenna system, the sheath reactance is much greater than the radiation resistance. Since the system is ultimately limited by the antenna voltage, the driving current is controlled by the sheath reactance. As it is shown in Section 4.1 that the wave amplitudes are proportional to the current, one way to increase the wave power is to reduce the sheath reactance. To reduce the sheath reactance, from equation (2), one can increase the physical size of the antenna, again, increase the operation frequency, and/or place the transmitter in regions of higher density by reducing the sheath thickness.

An alternative way to reduce the sheath reactance is to use a capacitance-loaded antenna structure. We have investigated this possibility. If an antenna is loaded with a pair of round plates at the ends of the antenna, the sheath reactance becomes

$$|X_s| \approx \frac{1}{4\omega A}\sqrt{\frac{2V_a}{\varepsilon_0 e N_0}}$$

(3)

where A is the area of the plate.

This requires a significantly large end-structure. Again, operation at higher frequencies in higher density regions can reduce the sheath reactance.

The zeroth-order theoretical analysis for simple antenna shapes is finished. However, the results have to be verified by experiments to be discussed below. The processes of sheath

near the satellite body have not been studied. For antennas of other shapes, such as that of Cygnus, numerical studies may be necessary in the future.

## 4.3    Space-borne VLF Transmission Experiments

The theoretical treatments of the plasma sheath processes discussed above benefited from some earlier work, e.g. Shkarofsky [1972]. However, the validity of our and previous models has not been tested. In our investigations we have identified some errors in these models. In addition, our physical understanding as described above, in particular the sheath current, is substantially different from earlier models although the mathematical treatments may have some similarity and our results recover earlier results under some extreme situations. In order to verify the theoretical models, we have conducted an experiment using the Radio Plasma Imager (RPI) on the IMAGE satellite [Reinisch et al., 2000] to transmit whistler waves in the inner magnetosphere using a set of tuning inductors. The RPI antenna is cylindrical which is the same as those modeled in theory. Figure 17 shows the measurements for one of such transmission periods. Clear enhancements in the current and voltage amplitudes are seen at some frequencies. The RPI was not designed for such operations, and it was necessary to make a slight change in transmission frequency in this experiment for each new inductor. Therefore, the frequency and inductance effects are intertwined. On top of that, the plasma conditions varied as the satellite moved from one region to another. One thing that is most striking is the positive correlation between the amplitudes of the antenna current and voltage. RPI does not measure the phase between the two. The product of the current and voltage is much greater than the radiated power because the sheath reactance is much greater than the radiation resistance, which is in series, resulting in a nearly 90° phase shift between voltage and current. We believe that the antenna is "in-tune" when these maximum amplitudes are measured. The in-tune condition is when $LC = 1/\omega^2$, where L, C, and $\omega$ are the tuner inductance, sheath capacitance, and the transmission angular frequency. Figure 18 shows the current as a function of equivalent capacitance if the circuit is in-tune. A clear concentration, peaked around 550 pF, of the in-tune conditions appears in a range of the equivalent capacitance. However, there is a spike, near 200 pF, away from the main peak. We are still in process of analyzing these data in order to understand the

factors that affect the in-tune conditions. Based on the results, we will then design a new RPI/IMAGE experiment, which will use a different frequency-inductance relationship aimed to reduce the uncertainty in the interpretations because the uncertainty, greater than a factor of 2 in the first experiment, may be large enough for more than one competing model to be valid.

X-Antenna current, [mA]

+X Antenna voltage [Volts]

-X Antenna voltage [Volts]
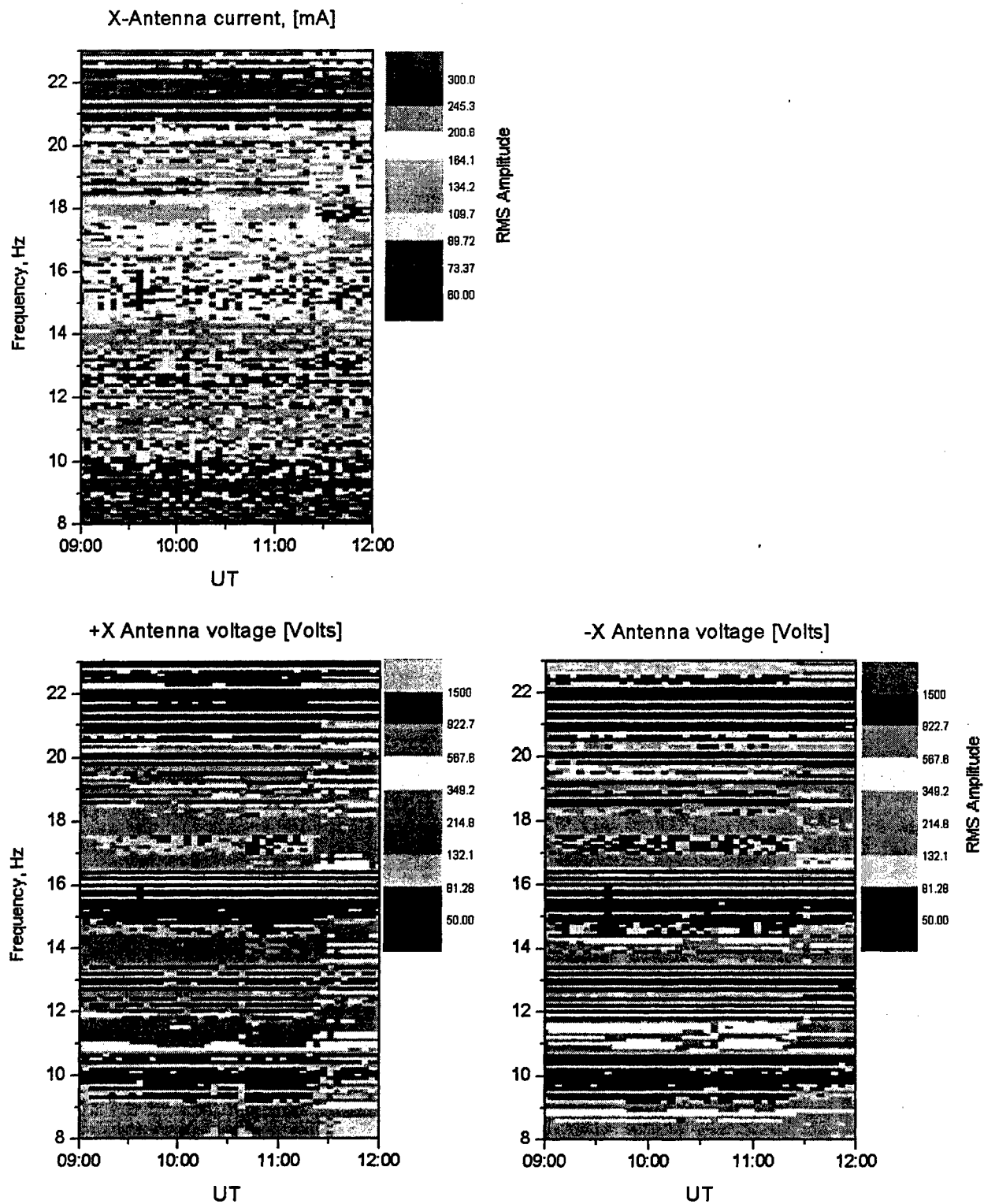
Figure 17. Current and Voltage on the X-antenna, Measured by RPI on 29 October 2004, During a Whistler Wave Transmission Experiment.

29
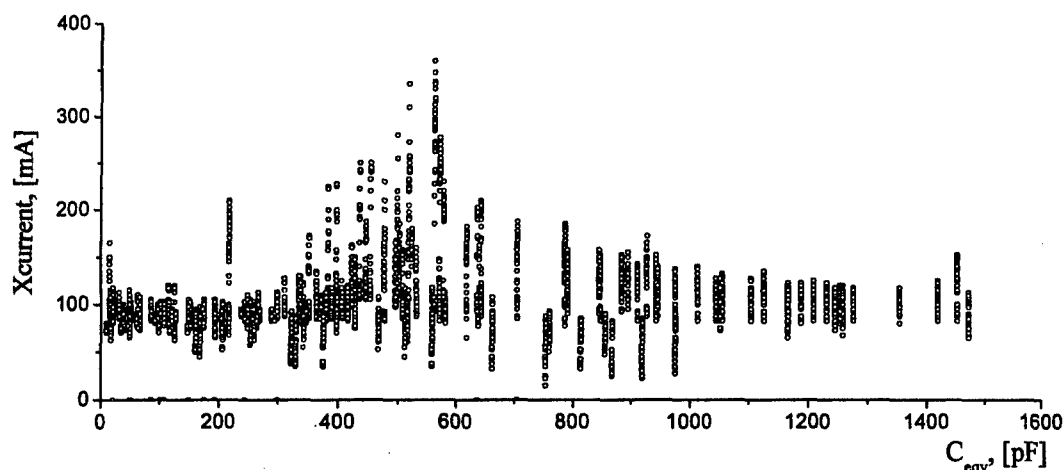
**Figure 18. Current in the X-antenna as a Function of the Equivalent Capacitance $C_{eqv} = 1/\omega^2 L$ for the 29 October 2004, Experiment Shown in Figure 17.**

## 4.4    Transmitter Conceptual Designs

With the physical understanding of the major processes, we have developed strategies to address each of the critical issues. These include the strategy for electric grounding, coupling methods between the antenna, circuits, and satellite, the concept of adaptive tuning, and a numerical simulation model of the electric circuit system.

Our study of the tuning system has ruled out the possibility of the dynamic tuning concept, which conducts tuning many times during a single wave cycle, because there is no electrical component available that operates at the required speed under the required high voltage with the adequate lifetime. The adaptive tuning concept would use nonlinear feeding so that the driving voltage becomes a square-wave. Since the two sheaths are in series, see Figure 10, a single value of total tuning inductance is adequate to tune the system most of the time except for the short intervals when the voltage reverses.

In order to simulate the system for design purposes, we have developed a numerical model that simulates the time dependent responses for a system similar to that in Figure

15. This model is crucial to our adaptive tuning concept because the signals are not sine waves. Figure 19 shows an example of the results. This model is still being improved and validated.
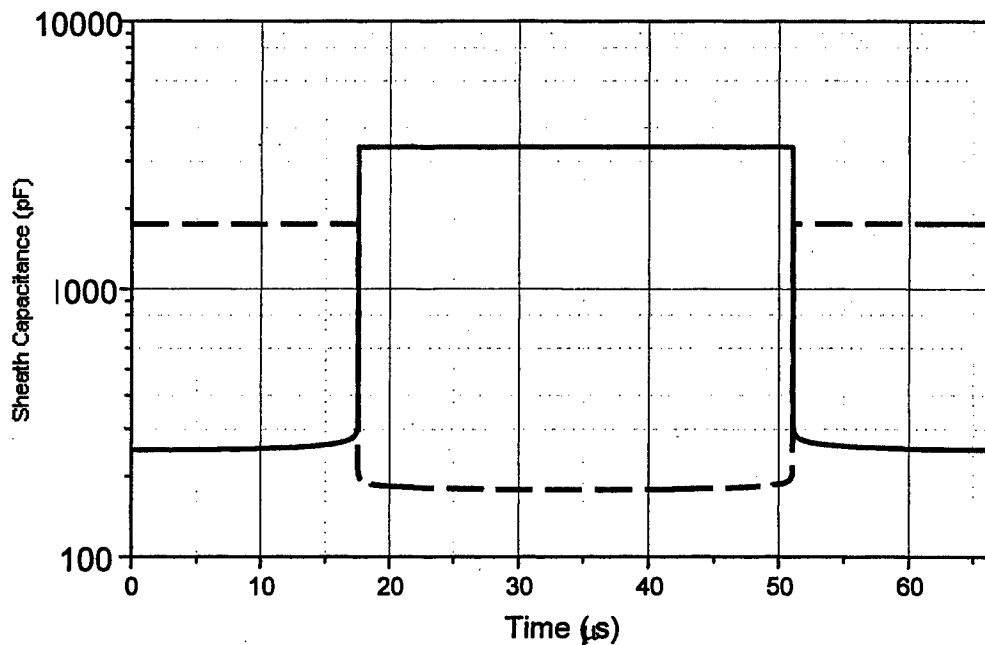


Figure 19. Calculated Sheath Capacitance for RPI Radiating System's X-dipole Antenna with Unequal Lengths, L1=250 m (dashed) and L2=125 m (solid) at 15 kHz. The Time Scale Represents One Period of the Radio Frequency. fpe = 100 kHz, fce = 300 kHz.

# 5 HAARP CAMPAIGN

## 5.1 Introduction

During two HAARP heating experiments on 22 and 23 March 2004 extending from 23 UT until about 04 UT the digisonde at Gakona, Alaska operated in the ionogram and "drift" mode in cooperation with other radar and optical observations. The radar transmitter and antenna array were used for transmission during the digisonde drift mode observations. In this drift mode, the digisonde is able to detect the spatial (horizontal) distribution of ionospheric (F-region) irregularities using the so-called skymap format.

31

During both campaigns the HAARP heater was operated on a 5-minute on and 10-minute off cycle at an RF frequency that varied as the F-layer critical frequency changed.

## 5.2    Campaign Results

On 22 March, the experiment began with the heater operating at 4.95 MHz and was changed to 5.80 MHz after 0330 UT (105 minutes after 0145 UT). On the 23 March campaign, the frequency was 5.80 MHz for the entire time from 0235 UT. For alternate heating periods that are with a 15-minute period the heater beam was pointed either vertically or in the magnetic zenith direction that lies approximately 15 degrees magnetically south of the overhead direction. Figures 20 and 21 show the magnetic north/south distribution of ionospheric irregularities as seen on the digisonde skymaps while operating in the drift mode.
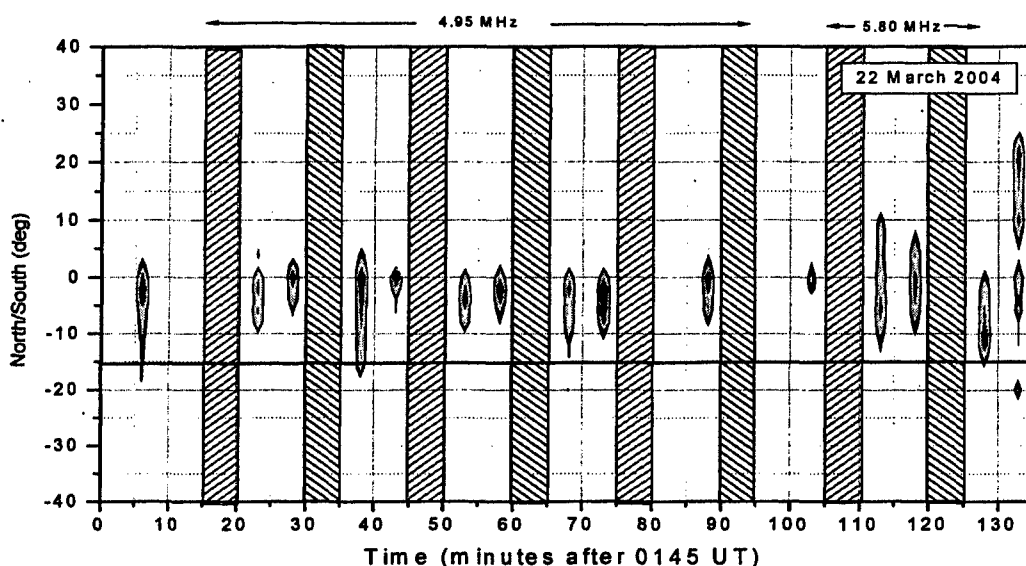


Figure 20. The Magnetic North/South Distribution of Digisonde Skymap Sources Observed During March 22, 2004 Heating Campaign. The Hatched Vertical Bars ▨ Indicate Overhead Heating and theOppositely Hatched Bars ▨ Magnetic Zenith Heater Direction (15 degrees off vertical).

Two skymaps were made during each 10-minute off period. The distribution of sources (irregularities) for each skymap was constructed by compressing the source locations in the east/west direction, leaving only the north/south distribution. Both figures show the persistence of overhead (0 degree) structures, essentially independent of the direction of

32

the heater beam. Most likely, these are naturally occurring irregularities, even appearing before the beginning of the heater transmissions.

On 22 March (Figure 20), there is a clear indication of the generation of ionospheric irregularities in the magnetic zenith direction following the 5-minute magnetic zenith-heating period from 0215 to 0220 UT. This effect appears to last less than 5 minutes, by the second drift cycle within the 10-minute off-period magnetic zenith heating irregularities are not apparent. On subsequent magnetic zenith heating cycles, the appearance of these irregularities is not as certain though there is an indication of a tendency to generate these magnetic zenith irregularities when the heater beam is pointed off-vertical as compared to when the heater is directed vertically.
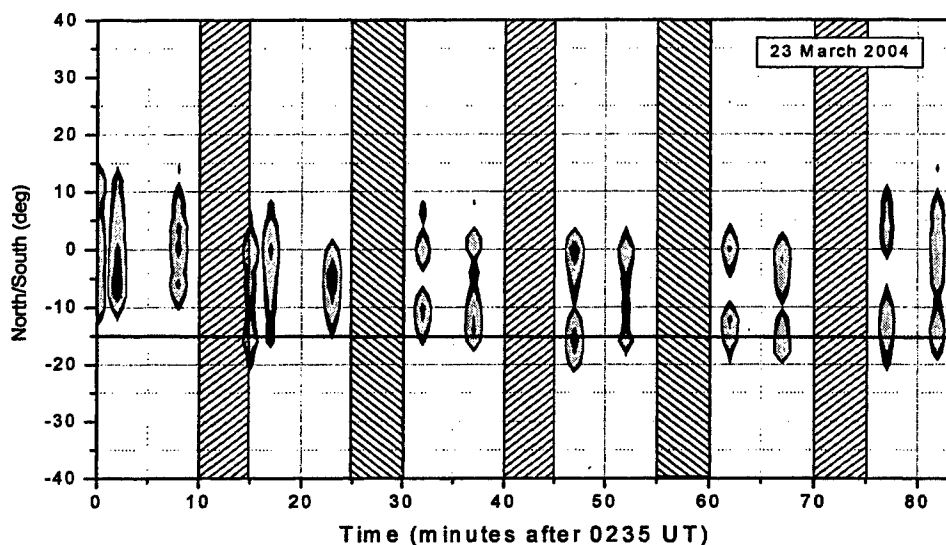


Figure 21. The Magnetic North/South Distribution of Digisonde Skymap Sources Observed 23 March 2004 Heating Campaign. The Hatched Vertical Bars ▨ Indicates Overhead Heating and the Oppositely Hatched Bars ▨ Magnetic Zenith Heater Direction.

On 23 March, the situation is significantly different. Here, in addition to the persistent overhead irregularities, there appears to be an additional distinct distribution of irregularities in the magnetic zenith that changes very little when the heater is directed either vertically or towards the magnetic zenith. At this point it is difficult to understand

33

the strong persistence on this night and there is a need to investigate differences on the two nights that might be important. A forthcoming paper by Djuth et al. [2005] discusses details.

Figure 22 shows the riometer absorption measurements at Gakona from 21 March through 23 March 2004. On 22 March during the first experimental program, the absorption was relatively low (see the first white band), of the order of 0.1 to 0.2 dB at 30 MHz, however on 23 March (second white band) there was only a relatively narrow window around 0230 UT when the 30 MHz riometer-absorption was of the order of 0.5 dB. During most of this second campaign the measured absorption was above 1 dB at 30 MHz, which transforms to $\approx$ 34 dB at 5.8 MHz (assuming $f^2$ dependence for D-region absorption).
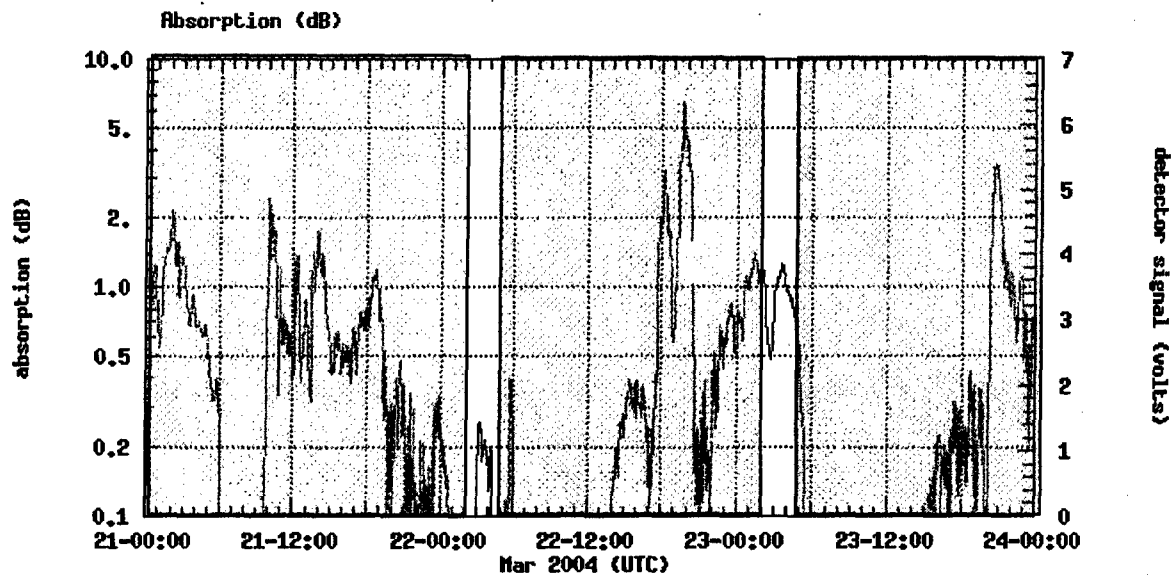


Figure 22. Riometer Absorption on 22 and 23 March 2004. The White Bands Indicate the Campaign Periods on 22 and 23 March. (Source: www.haarp.alaska.edu)

Another issue that has been examined is the relationship between the heater frequency and the F-layer critical frequency during the two campaigns. Figure 23 shows the measured foF2 values during both campaigns. The two white bands are the heater

34

operation periods on the two nights and the horizontal dashed lines indicate the heater operating frequencies. On 22 March, from 0200 to 0320 UT the heater operated at 4.95 MHz that was approximately 1 MHz below the F-layer critical frequency. At 0320 UT, the heater frequency was raised to 5.80 MHz, very close to foF2. A short time after 0320, the heater frequency actually exceeded the critical frequency of the F-layer and heating became relatively ineffective. The skymaps following the 0315 to 0320 UT heating cycle shows no sources (echoes) which is consistent with $f_{htr} >$ foF2. The skymap observations used the same frequency as the heater, i.e., $f = f_{htr}$.

On 23 March, the heater frequency at 5.80 MHz was consistently below foF2, though the frequency separation varied during the experiment. These variations of foF2 appear to have no relationship to the persistence of the magnetic zenith irregularities.
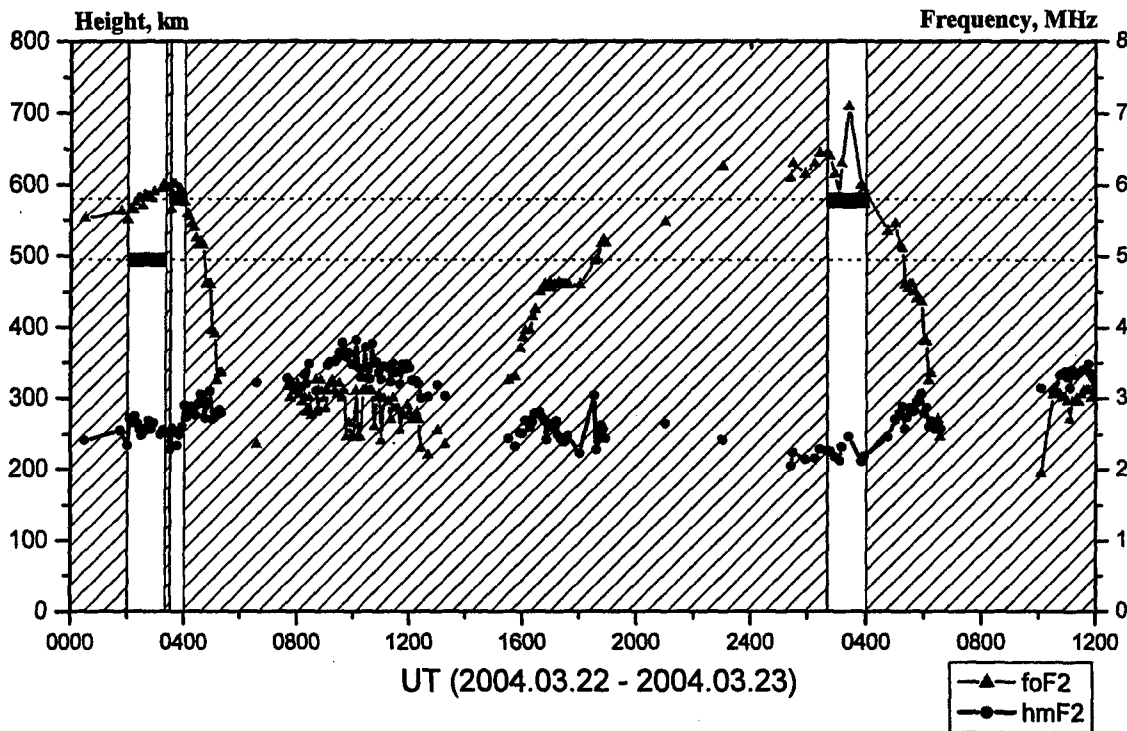


Figure 23. foF2 and hmF2 at Gakona, Alaska for 22-23 March 2004. White Vertical Bands Indicate Time Periods for the Two HAARP Campaigns. The Horizontal Black Bars Indicate the HAARP Operating Frequencies During Each Campaign.

## 5.3 HAARP Digisonde Upgrade

A new DPS-4 was constructed as an upgrade for the HAARP digisonde. The objective was to achieve better reliability and to modernize the installation to permit all the latest software to perform optimally. It was installed by UMLCAR personnel in December 2004. Many spares including all the computer parts were also delivered.

## 6 DRIFT SOFTWARE DEVELOPMENT

### 6.1 Introduction

A *Fortran*-based software package (Digisonde Drift Analysis, or DDA) for analysis and visualization of the digisonde data collected in the so-called drift mode had been developed and maintained at UMLCAR in 1980-1990. A critical decision of using the *Java* language as the preferable language for digisonde-related applications was made in 1998. In 2002 it was agreed to start a new spiral of drift software development based on the *Java* language/technology. At that time we already had two large databases with *Java* applications. From the very beginning we clearly understood important advantages of the *Java* language over both *Fortran* and *C++*. This language allows creating a more understandable and yet still complex and more reliable architecture than *C++*. *Java* is extremely portable, - a compiled version of the application should work under any operating system, provided a computer has a *Java machine*. *Java code* is dynamically loaded and it allows creating a very large application – executable code may contain tens of megabytes without a problem. This unique feature of Java has made it possible to centralize all drift analysis/representation functionality in one principal application. One additional important feature of *Java* is its standard interface for *database* access, called the *JDBC* interface.

### 6.2 Content

Presently, the following Java-based applications for digisonde drift analysis exist:

DriftExplorer. (Figure 24) This is the principal application for drift processing. It provides a wide spectrum of possibilities to the digisonde users. It is also the main testing area for developing *Java* class library for drift data processing and *database* access.
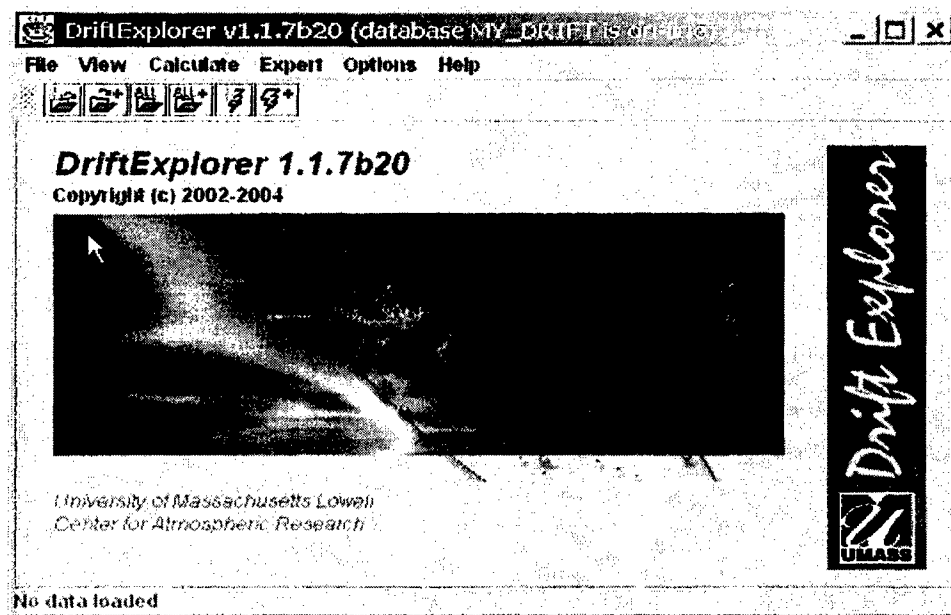
**Figure 24. DriftExplorer Start Window**

**Sky2Png.** This application produces skymap plots and is specifically designed for digisonde unattended console mode operation like the DISS environment. As it uses the same classes as DriftExplorer, it has the identical capabilities to DriftExplorer in reading and representing skymap data.

**Dvl2Png.** This program produces plasma drift velocity plots and is designed for digisonde unattended console mode operation as well. As it uses the same classes as DriftExplorer, it also has the identical capabilities to DriftExplorer in reading and representing drift velocity data.

**FillDriftData.** This is an "invisible" application dedicated to filling the Drift database with drift data. It usually works in persistent 24x7 console mode but it can also work in batch mode or even in graphical interactive mode.

**DriftBase or Drift database.** This is a database containing raw drift data as well as plasma drift velocity and skymap data derived from the raw drift data. At the initial phase of the drift software development project this database was only capable of keeping velocity data, but in 2004 it was revisited and a new version of DriftBase was set up.

37

## 6.2.1 DriftExplorer

Described here are some of the key features of the DriftExplorer application.

### Data loading

DriftExplorer allows loading the data from files and/or from DriftBase. The loading operation does not actually put the data into computer memory but instead creates a list of records with each entry corresponding to some real data record. DriftExplorer also keeps information about station, time, and the storage location of this record. This approach allows us to minimize memory requirements by loading a data record when it is required (e.g., viewing, calculation etc.) and immediately unloading it when it is no longer necessary to keep it in memory. Another implemented approach for memory requirement minimization consists of keeping only one memory buffer for data record while allowing several threads for processing.

If the user has already loaded some data, so that the list of stations and lists of the data records are available, then it is possible to either reload new data eliminating all previously loaded lists, or to add some new data and keep previously loaded lists.

### Current station and current record

In the DriftExplorer main window one always sees *current station* and *current record* shown in the station and record combo boxes. Next to these boxes a common record navigation bar is available. The user can change *current record* or/and *current station* by using either of these controls. Record combo box identifies *current record* of *current station* by time and also shows what types of data are loaded for each record. Examples of *current station* and *current record* are shown in Figure 25.
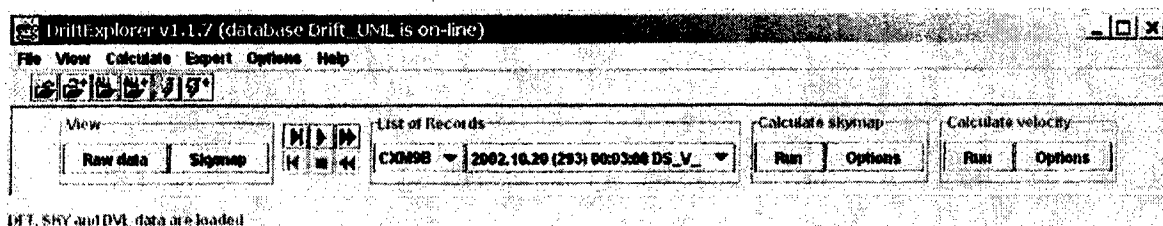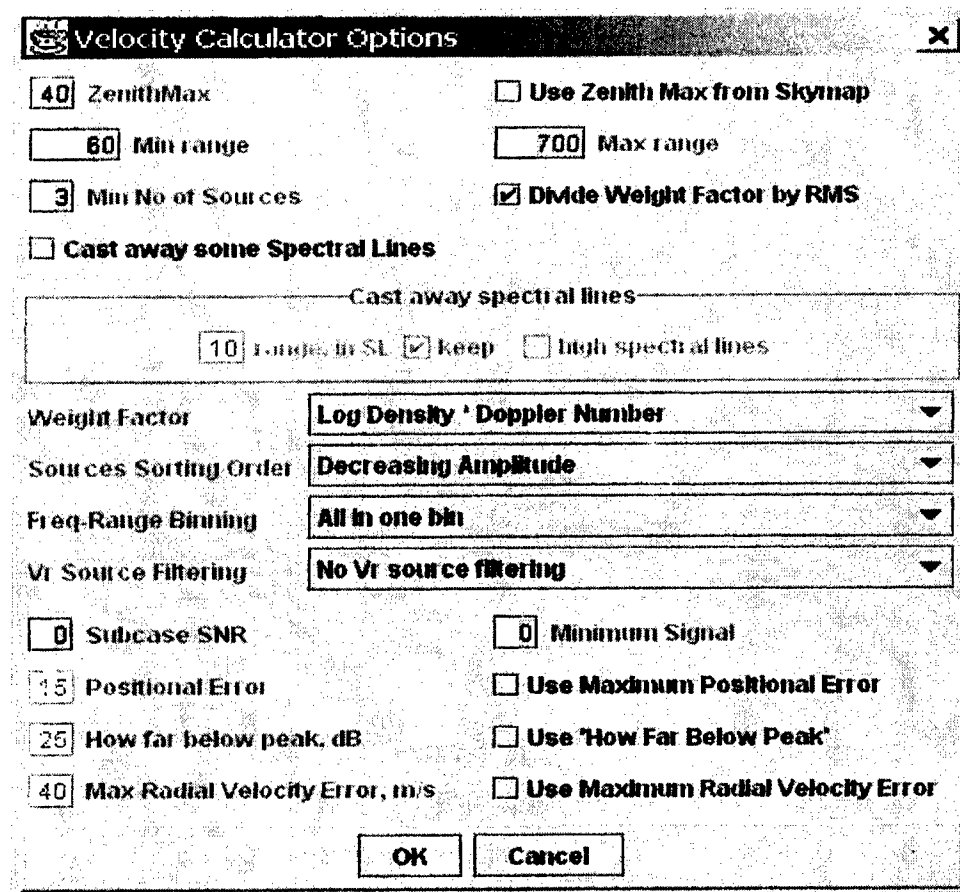


Figure 25. DriftExplorer Main Window

**Data navigation and viewing**

Raw drift, skymap and plasma velocity data can easily be navigated and viewed by opening a *view window*. Each type of data has its own type of *view window*. The user can open one or more *view windows* for each data type. Each *view window* has its own navigation controls that contain station and record combo boxes where one can choose station and record directly. Raw data and skymap *view windows* also contain a record navigation bar, which allows a user to browse through data records. It is also possible to open one *synchronized view window* for both raw drift and skymap data. Navigation controls between raw drift and skymap *synchronized view windows* and main window are synchronized, so any of them can be used for navigation. All other *view windows* are called *unsynchronized* and are navigated independently.

**Skymap plots and plasma drift velocity calculations**

DriftExplorer allows the user to calculate skymaps and plasma drift velocities from raw drift data. Previously, these calculations were implemented through the external calls of the ddas.exe and ddav.exe executables, which are a part of the DDA package. All the parameters necessary for these calculations can now be set in the DriftExplorer application. Note that each digisonde station has its own list of parameters that is kept in an external file. The skymaps and velocities (Figure 26) can be calculated either for a single data record or for all data records loaded.

**Figure 26. Velocity Calculation Options**

### Drift database connection and accounts

To connect to the DriftBase (Figure 27) a user needs *Database URL*, *User name* and *Password* that should be entered in the menu item Database connection under the File menu. The DriftBase currently allows the users not only to read the data but also to add new data. To be able to submit the data into the DriftBase one has to be logged in as an "Expert". This can be done with the use of the menu item Login in the Expert menu. Each Expert can only save and/or modify data in the DriftBase submitted under his/her name.
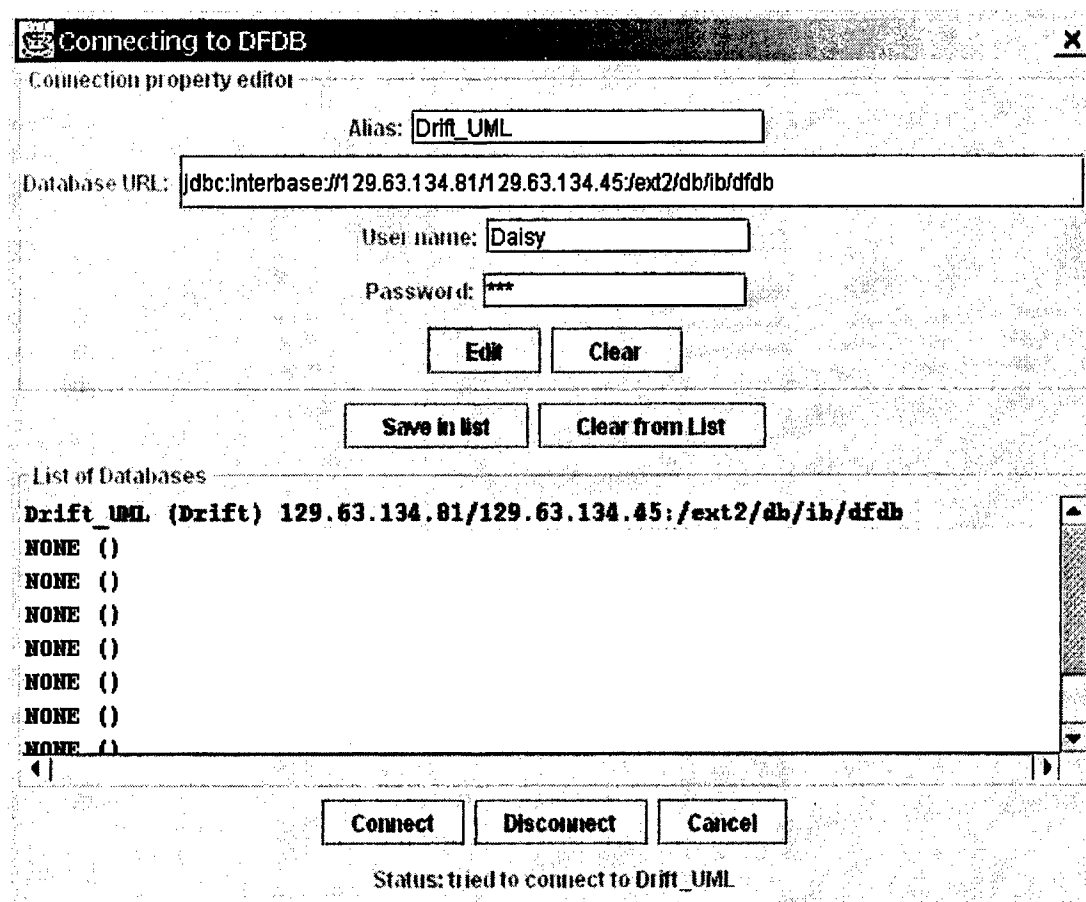
**Figure 27. Connecting to DriftBase**

## Exporting data

DriftExplorer allows the user to export any type of data, saving it in external files. It is possible to save a single *data record* as well as a whole data set loaded. Before closing the application or before loading a new data set, DriftExplorer reminds the user to save all the data that have been modified after loading. *Experts* can also automatically submit calculated skymap or velocity data in the DriftBase using automatic submit option.

## View window

All types of *view windows* have some common navigation controls. It is possible to maximize the viewable region of *view window* by removing all control panels from it, 'Window size image' from a pop-up menu should be chosen. 'Normal size image' option allows returning back to the original window size. Two color schemes for the plots are available: 'screen color scheme' with a black background and 'printer color scheme' with

41

a white background. The view window can be saved as an image in either *png* or *gif* format. The user has a full control over the plot parameters that allows him/her to produce an optimal image depending on the type of presentation required.
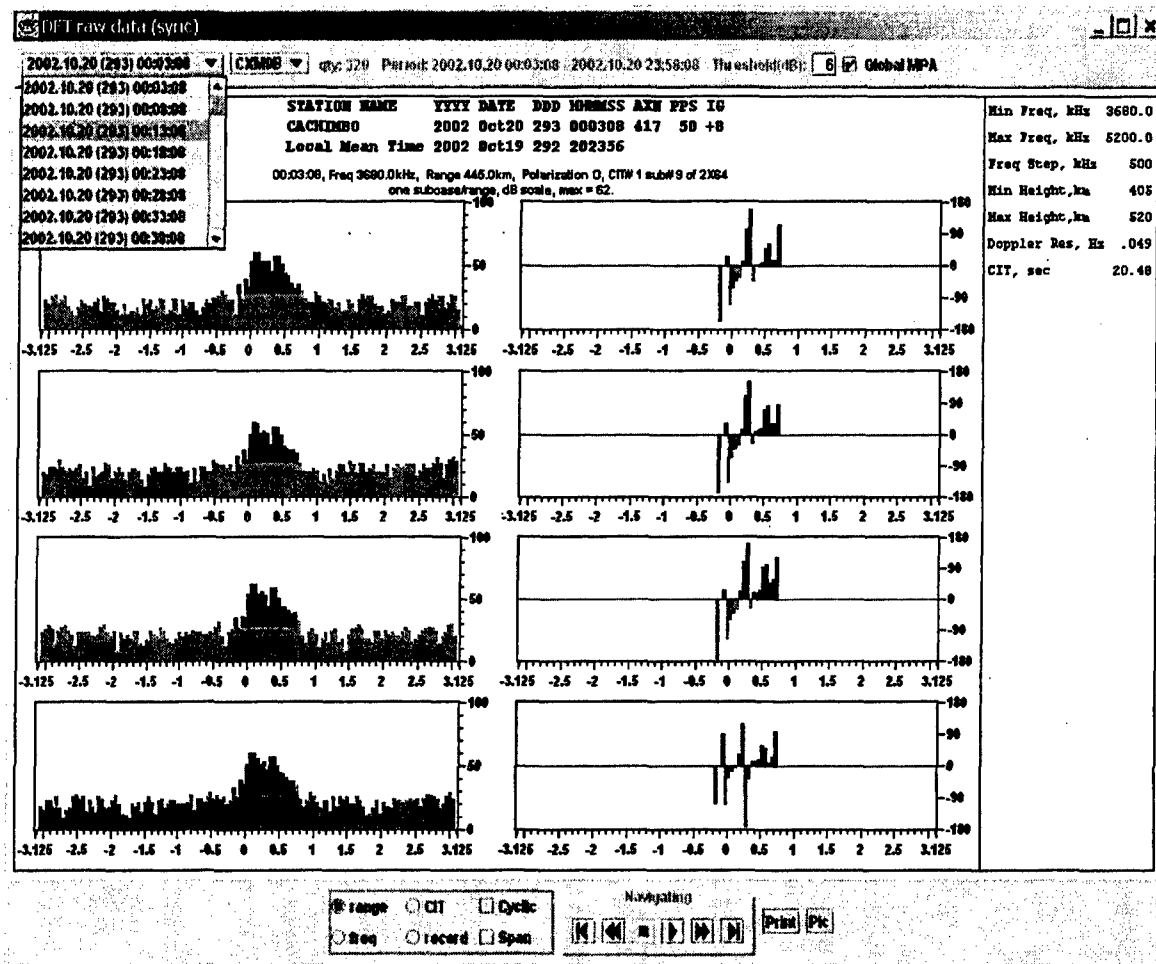


Figure 28.  DFT Raw Data (sync), Amplitudes (left) and Phases (right) for the Four Antennas

## Drift data view window

This window can show a single data record in two presentations: amplitude and phase spectra (Figure 28) for all antennas or a so-called waterfall plot (Figure 29), where amplitude spectra are shown for a single frequency and all height ranges available. DriftExplorer allows the user to optimize the presentation of the raw data by selecting an amplitude threshold values and amplitude scales. It is also possible to select from a variety of navigation options, *i.e.*, to browse the data through different height ranges,

42

operating frequency, polarization, or integration cycles available within a single data record (Figure 30).
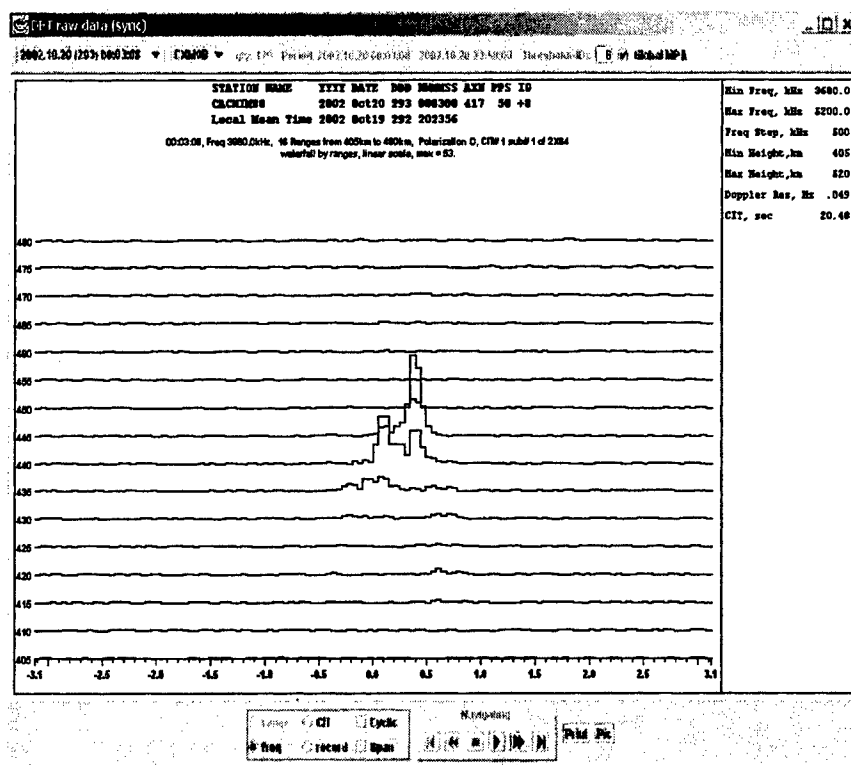


Figure 29. DFT Raw Data. Waterfall Display of all Range Gates for Selected Frequency
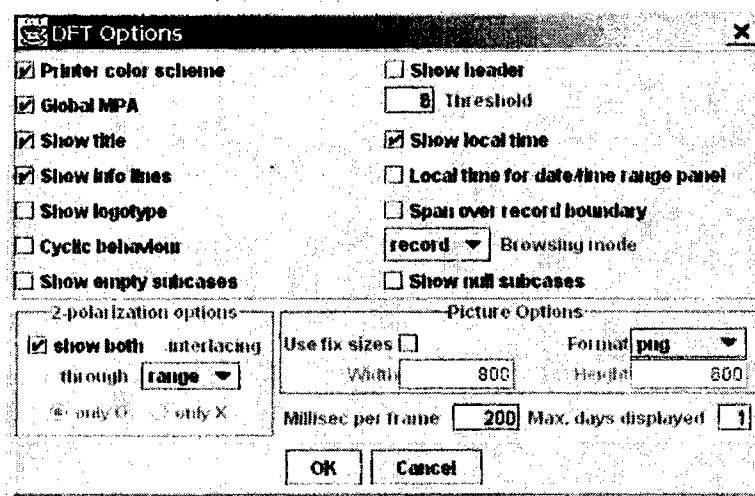


Figure 30. DFT Options

## SKY data view window

This window displays one data record at a time. This plot type shows the locations of all points in the ionosphere (traditionally called 'source'), from which the radio wave is

reflected back to the digisonde (Figure 31). Either amplitude or Doppler frequency shift can be color-coded for the source points. A number of options including selection of the data frequency, polarization, range interval, etc., are available to produce a desired presentation (Figure 32).
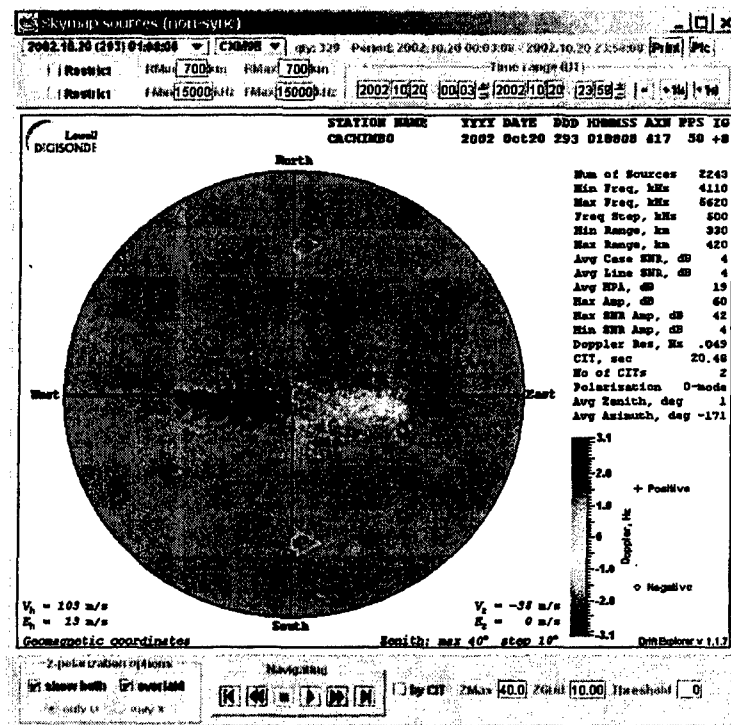


Figure 31. Skymap. The White Arrows Give the Calculated Horizontal Drift Velocity.
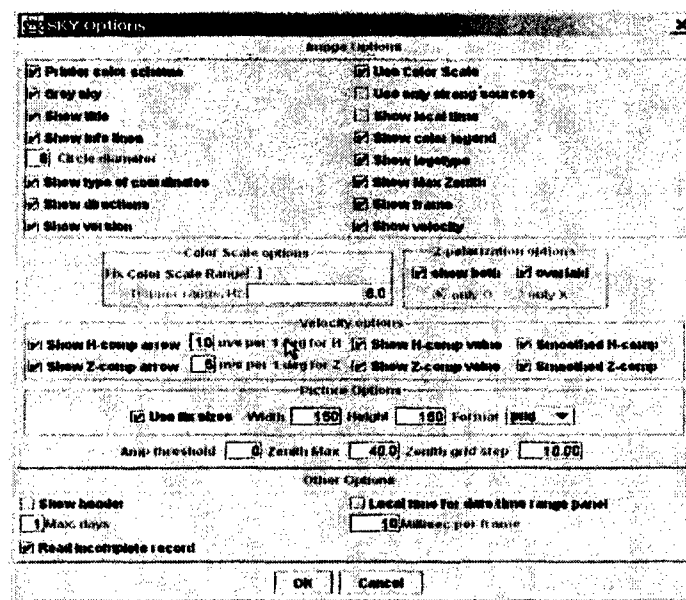


Figure 32. SKY Options

## Velocity data view window

This window shows a time series of calculated plasma drift velocities; with the velocity vector components presented either in Cartesian or cylindrical coordinate systems. Furthermore, the velocities can be calculated and shown in geographic, geomagnetic (see Figure 33), or corrected geomagnetic coordinates. Velocities shown in the plot are usually smoothed; it is also possible to select the parameters of the smoothing window. An interesting option - 'daily average' - allows the user to average the velocity data over a number of successive days (Figure 34). If velocity data for two or more stations for approximately the same period of time are loaded, then it is possible to compare velocities from two stations (Figure 35) by pushing the button 'Compare' (when only two stations are loaded), or choosing other stations from the list (if more than two stations are loaded). 'Daily average' and 'Compare' options can be used simultaneously (Figure 36).
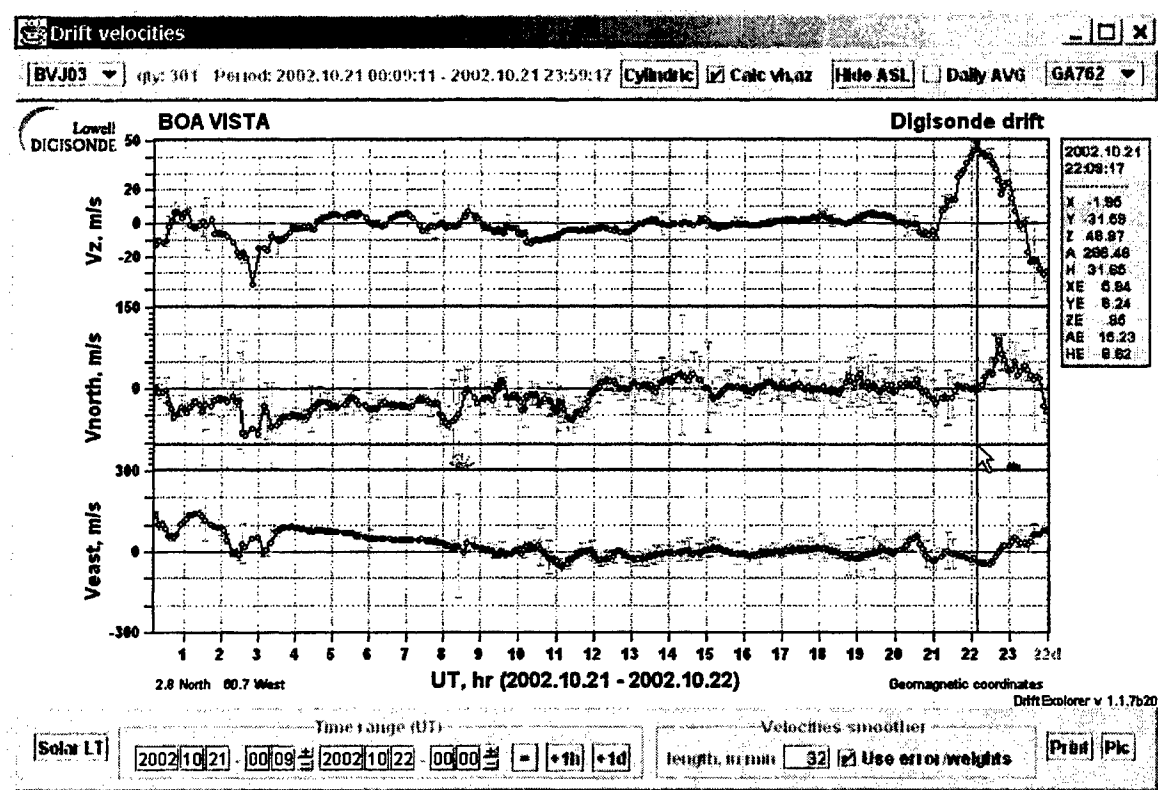


**Figure 33. Online Display of Drift Velocity Components for 21 October 2002. Error Bars are Shown in Gray.**
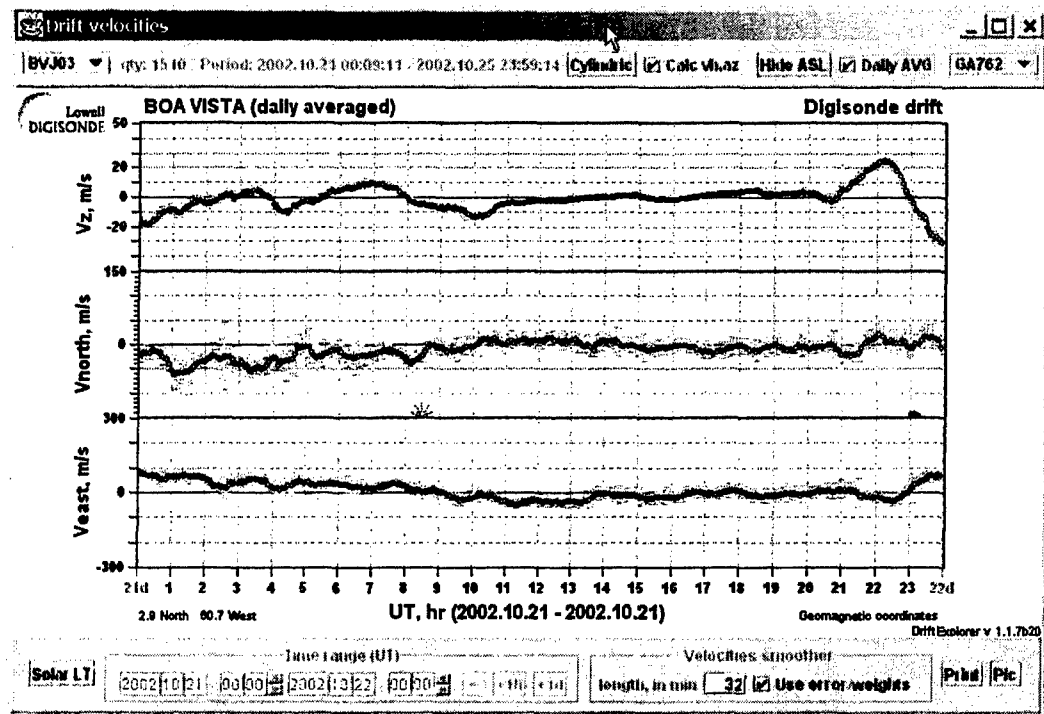
Figure 34. Velocity Components Averaged Over 5 days, 21-25 October 2005
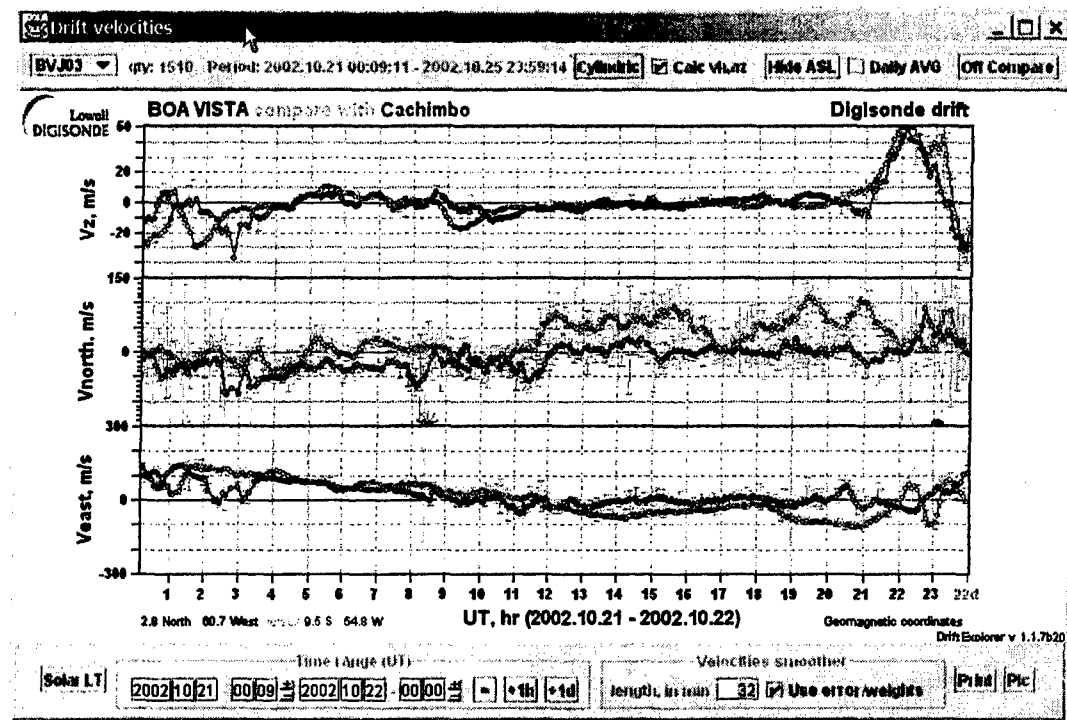


Figure 35. Comparing Simultaneous Drift Velocities at Two Sites.

46
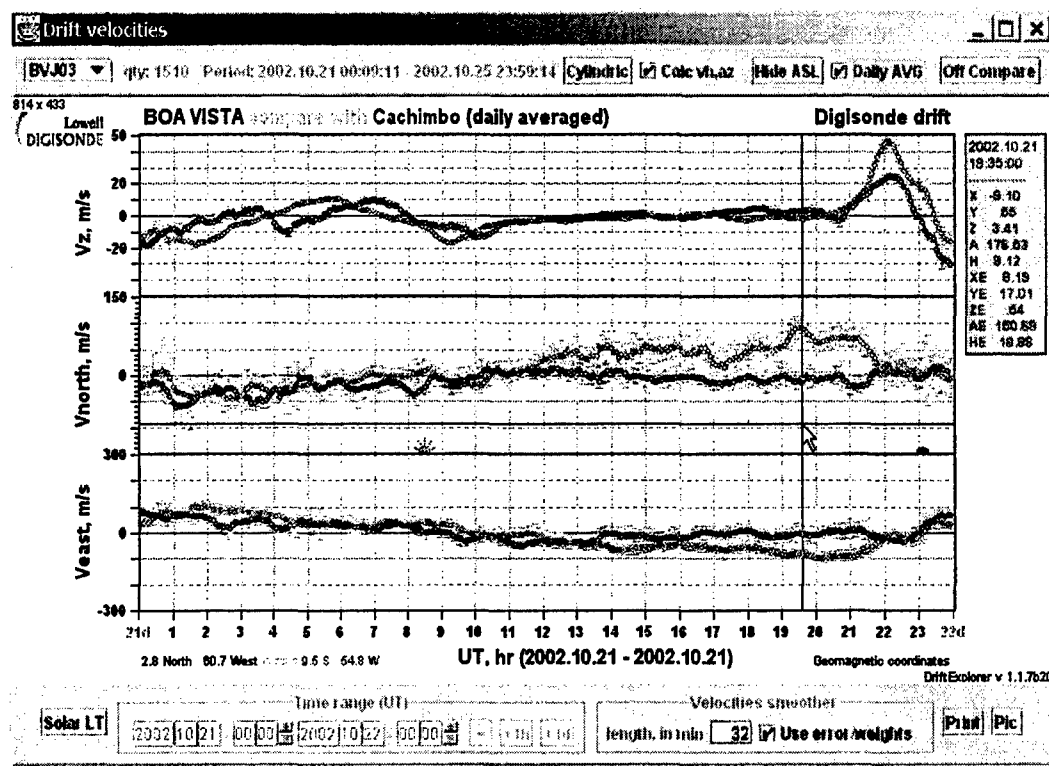
Figure 36. Comparing 5-day Average Drift Velocities at Cachimbo (equator) and Boa Vista
(Northern Anomaly)

## 6.2.2 Drift database

Drift database was implemented using the contemporary *open source* database Firebird
1.5. Here is a citation from an interview with Helen Borrie, an author of an excellent
book about the Firebird database.

*"It's a fork of a mature commercial database called InterBase. InterBase is an enterprise-level database -- Firebird is the same, but better. You'll find Firebird behind a number of Web sites, storing records for telecom companies and managing data for point-of-sales systems -- just about anywhere you might find Oracle or [Microsoft] SQL Server."*

*"Firebird is an open-source relational database, emerged from the InterBase source code, release by Inprise Corporation -- now known as Borland -- in 2000. Firebird, which runs on Linux, Windows and a variety of Unix platforms, offers concurrency, high*

47

*performance and powerful language support for stored procedures and triggers. It has been used in production systems under a variety of names since 1981."*

Here are the key features of the DriftBase.

- **Storing raw drift data and skymap data in their original formats.** This is exactly the same approach as the one used in the DIDBase [Reinisch et al., 2004], - preserving the original format of data whenever it is possible.

- **Possibility of storing more than one skymap and velocity data record for a single raw drift record.** Skymap and velocity data records are stored in the DriftBase with an attribute of an Expert who submitted them. So it is possible to keep several skymap and velocity records produced from the same raw drift record as each registered Expert may have his/her own skymap and/or velocity data records in the DriftBase.

- **Compressed format.** Raw data and skymap data are compressed before submission to the DriftBase, which allows saving about 40 % of disk space.

- **Supporting read-only users and expert users.** Two types of users (or *roles* in database terminology) are supported, read-only users (*role* COMMON) and expert users (*role* EXPERT).

- **Separation of blob data from the rest of the data in order to increase search speed.** Speed of database operation is one of the main issues for very large databases, so it requires additional attention of database administrators. In our case, blob data (= non-searchable data) occupy 95% of the database space, therefore, when a user is searching for something from the rest 5% of searchable data, his disk I/O operations (which are read-ahead operation by nature) will be probably 95% congested with blob data, assuming these 5% are uniformly spread. This problem is not so critical if enough computer memory is available or if the database is used very intensively so that all these 5% of searchable data are stored in computer memory cache. Separating blob data from other data also makes it easier to maintain the database.

- **Thorough design and implementation of *stored procedures.*** Among those *stored procedures* it is worth mentioning several ones related to the Drift database

navigation through the *Dynamical Navigating Tree* (Figure 37). It is helpful to think of the data as being organized in a tree-structure. Having such a thought tree in mind one can navigate faster and more rationally.
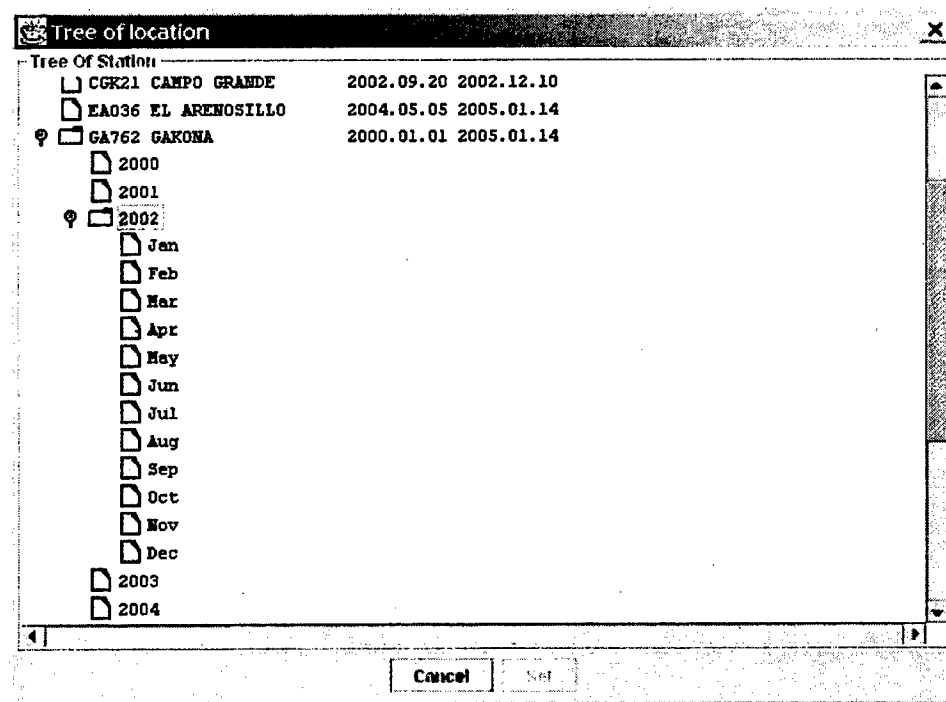


Figure 37. **Tree of Locations**

## 6.3    *Statistics*

Number of Java classes developed: $\geq 800$

Source code size: $\geq 2.7\,\text{Mb}$

DriftBase size: $\cong 90\,\text{Gb}$

(See also inventory of DriftBase shown in Table 2)


## 6.4    *Application*

DriftExplorer is already being intensively used at UMLCAR, as well as by other digisonde users. However, the potential and operational flexibility of the package and growing Drift database make it appealing for much wider and more intensive use.

The latest version 1.1.7 that includes all described features is released and can be downloaded from http://ulcar.uml.edu/Drift-X.html.

49

## 6.5    *Future work*

- Add new types of data representations

- Improve processing control flexibility

- Add skymap statistics calculation, visualization, and storage in the DriftBase

- Rewrite ddas.exe, ddav.exe programs in Java language and implement certain suggested improvements in the calculation algorithms, including the Generalized Digisonde Drift Analysis (GDDA) algorithm.

Table 2. Drift Database Inventory on 10 January 2005

| URSI | Year | Jan | Feb | Mar | Apr | May | Jun | Jul | Aug | Sep | Oct | Nov | Dec |
|------|------|-----|-----|-----|-----|-----|-----|-----|-----|-----|-----|-----|-----|
| AN438 | 2004 | | | | | | | | | | | 17 | 31 |
| AN438 | 2005 | 7 | | | | | | | | | | | |
| AT138 | 2003 | | | | | | | | | | | 21 | 31 |
| AT138 | 2004 | 31 | 26 | 30 | 30 | 31 | 30 | 31 | 31 | 30 | 28 | 30 | 31 |
| AT138 | 2005 | 13 | | | | | | | | | | | |
| BVJ03 | 2002 | | | | | | | | | | 27 | 19 | 9 |
| CAJ2M | 2002 | | | | | | | | | | 25 | 30 | 10 |
| CGK21 | 2002 | | | | | | | | | 11 | 31 | 30 | 10 |
| CXM9B | 2002 | | | | | | | | | 3 | 31 | 30 | 10 |
| EA036 | 2004 | | | | | 27 | 30 | 31 | 31 | 30 | 11 | 30 | 28 |
| EA036 | 2005 | 13 | | | | | | | | | | | |
| EB040 | 2004 | | | | | | | | | | | 2 | 31 |
| EB040 | 2005 | 13 | | | | | | | | | | | |
| GA762 | 2000 | 4 | 24 | 17 | 30 | 22 | 30 | 31 | 29 | 30 | 29 | 28 | 31 |
| GA762 | 2001 | 31 | 28 | 31 | 6 | 23 | 30 | 29 | 22 | 23 | 26 | 30 | 30 |
| GA762 | 2002 | 16 | 26 | 31 | 29 | 30 | 30 | 31 | 30 | 30 | 31 | 30 | 31 |
| GA762 | 2003 | 21 | 3 | 20 | 21 | 31 | 30 | 25 | 27 | 30 | 31 | 29 | 30 |
| GA762 | 2004 | 31 | 29 | 31 | 30 | 30 | 26 | 29 | 29 | 29 | 17 | 24 | 31 |
| GA762 | 2005 | 13 | | | | | | | | | | | |
| GSJ53 | 2004 | | | | | | | | | | | 2 | 31 |
| GSJ53 | 2005 | 5 | | | | | | | | | | | |
| JI91J | 1993 | | | | | | | 11 | 31 | 27 | 28 | 30 | 27 |
| JI91J | 1994 | 31 | 28 | 30 | 7 | 12 | 29 | 28 | 31 | 24 | 23 | 30 | 31 |
| JI91J | 1995 | 31 | 28 | 30 | 30 | 31 | 6 | | | 9 | 26 | 11 | |
| JI91J | 1996 | | | 17 | 31 | 29 | 26 | 28 | 30 | 24 | 29 | | 31 |
| JI91J | 1997 | 21 | 28 | 26 | 23 | 31 | 30 | 31 | 31 | 30 | 31 | 26 | 31 |
| JI91J | 1998 | 31 | 26 | 27 | 29 | 29 | 1 | 11 | 21 | 29 | 30 | 28 | 26 |
| JI91J | 1999 | 29 | 25 | 25 | 28 | 28 | 28 | 31 | 30 | 28 | 28 | 29 | 28 |
| JI91J | 2001 | | | | | | 25 | 23 | 2 | 21 | 31 | 30 | 31 |
| JI91J | 2002 | 31 | 27 | 31 | 30 | 31 | 30 | 29 | 31 | 30 | 28 | 30 | 29 |
| JI91J | 2003 | 31 | 28 | 30 | 30 | 31 | 29 | 28 | 31 | 28 | 29 | 30 | 31 |
| JI91J | 2004 | 31 | 28 | 31 | 30 | 31 | 26 | 31 | 31 | 28 | 15 | 25 | 13 |
| KS759 | 2004 | | | | | | | | | | | | 1 |
| MHJ45 | 2002 | | | | | | | | | | 31 | 15 | |
| MHJ45 | 2003 | | | 20 | 14 | | 12 | 31 | 31 | 30 | 31 | 15 | 31 |
| MHJ45 | 2004 | 31 | 28 | 31 | 30 | 31 | 30 | 31 | 31 | 28 | 17 | 30 | 31 |
| MHJ45 | 2005 | 13 | | | | | | | | | | | |
| PA836 | 2004 | | | | | | | | | | | | 1 |
| PQ052 | 2004 | | | | | | | | | 15 | 18 | 22 | 19 |
| PQ052 | 2005 | 1 | | | | | | | | | | | |
| SAA0K | 2002 | | | | | | | | | | 25 | 13 | |
| SAA0K | 2003 | | | 30 | 30 | 31 | | | | | | | |
| SMJ67 | 2004 | | | | | | | | | | | 2 | 31 |
| SMJ67 | 2005 | 13 | | | | | | | | | | | |
| THJ77 | 2002 | 1 | 1 | 1 | | | | | | | | | |
| THJ77 | 2003 | | | | | | | | | | | 19 | 31 |
| THJ77 | 2004 | 31 | 28 | 31 | 29 | 31 | 30 | 31 | 31 | 30 | 15 | 30 | 31 |
| THJ77 | 2005 | 13 | | | | | | | | | | | |
| VT139 | 2004 | | | | | | | | | | | | 1 |

# 7    CAL/VAL PROJECT

## 7.1    *Introduction*

The DMSP (Defense Meteorological Satellite Program) F16 weather satellite was launched on 18 October 2003. It has two optical instruments onboard:

1.  SSULI - limb scanning ultraviolet imager / spectrometer (built by the Naval Research Laboratory)

2.  SSUSI - nadir scanning ultraviolet imager /spectrometer and photometer (built by the Applied Physics Laboratory at Johns Hopkins University)

The satellite orbit is almost polar with a period of 101.9 min, apogee 853 km, perigee 843 km, and inclination 98.9°.

The digisonde ground-based electron density profiles serve as "ground truth" for the satellite-borne UV optical measurements of "F layer" and "auroral E layer" electron densities. Aerospace corporation was responsible for calculation of "fly over" events when satellite and digisonde can measure the same part of ionosphere. This includes surface scans and limb measurements. It gives up to 4 events per 24 hours period for each participating digisonde. Each event is a one hour interval for which UMLCAR is to provide manually scaled ionospheric data in SAO 4.3 format with 15 minutes cadence (can be different for non-DISS network digisondes). 27 digisondes around the world were engaged in the cal/val effort.

**Current CalVal station list:**
(**bold** = non-DISS digisonde stations)

| 01 | AS00Q | ASCENSION ISLAND | |
|----|-------|------------------|------|
| **02** | **AT138** | **ATHENS** | Greece |
| **03** | **BV53Q** | **BUNDOORA (some data)** | Australia |
| **04** | **CAJ2M** | **CACHOEIRA PAULISTA** | Brazil |
| **05** | **DB049** | **DOURBES** | Belgium |
| 06 | DS932 | DYESS AFB | Texas |
| 07 | EG931 | EGLIN AFB | Florida |
| **08** | **EA036** | **EL ARENOSILLO** | Spain |
| 09 | FF051 | FAIRFORD | U.K. |
| **10** | **FZA0M** | **FORTALEZA (delayed data)** | Brazil |
| **11** | **GR13L** | **GRAHAMSTOWN** | South Africa |
| **12** | **HA419** | **HAINAN** | China |
| **13** | **JI91J** | **JICAMARCA** | Peru |

| 14 | JR055 | JULIUSRUH | Germany |
| 15 | LM42B | LEARMONTH | Australia |
| 16 | MU12K | MADIMBO | South Africa |
| 17 | MHJ45 | MILLSTONE HILL | USA |
| 18 | SN437 | OSAN | Korea |
| 19 | PSJ5J | PORT STANLEY | Argentina |
| 20 | PA836 | PT ARGUELLO | California |
| 21 | PRJ18 | RAMEY | Puerto Rico |
| 22 | PRJ18 | ROME | Italy |
| 23 | EB040 | ROQUETES | Spain |
| 24 | T139 | SAN VITO | Italy |
| 25 | SAA0K | SAO LUIS | Brazil |
| 26 | SMJ67 | SONDRESTROM | Greenland |
| 27 | WP937 | WALLOPS IS | Virginia |

## 7.2 Software development

In support of the campaign, UMLCAR has developed and tested a set of programs, including ADRES - Automated Data Request Execution System (Figure 38).
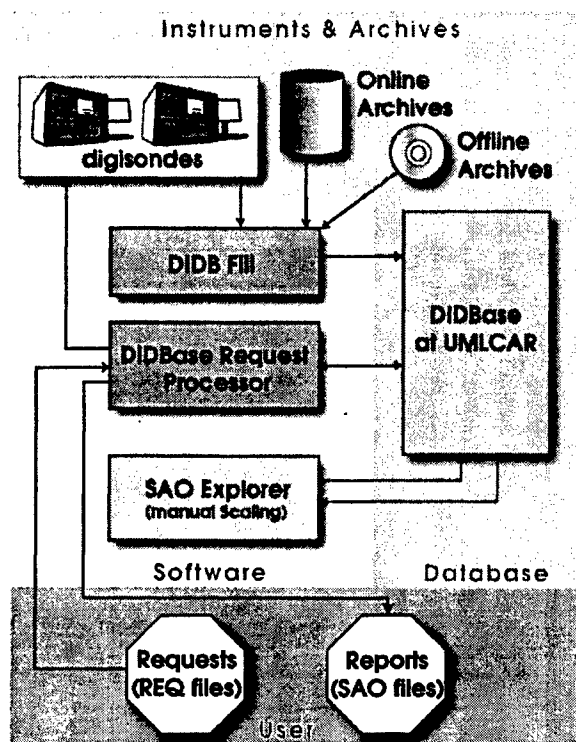


Figure 38. ADRES Flow Diagram

This year a new version of ADRES software has been released including DIDBFill program. The program is responsible for data ingestion onto DIDBase. It has been

53

designed to diagnose incoming data to avoid loading bad data with errors, incomplete, or "future" data.

DIDBReqPro program. This is major program of ADRES and

- handles incoming requests
- initiates DIDBFill program to load the data
- generates email messages to a scaler concerning data availability
- generates result reports and email messages to the requested party

The program has an improved data management logic and FTP download algorithm.

The SAOExplorer program has been improved to simplify work with requests. New "Role" - ADRES was added to DIDBase. New function "Next Request" has been implementing in the program. Using this, the scaler can load all requested ionograms for "one day"/station with one click (Figure 39).
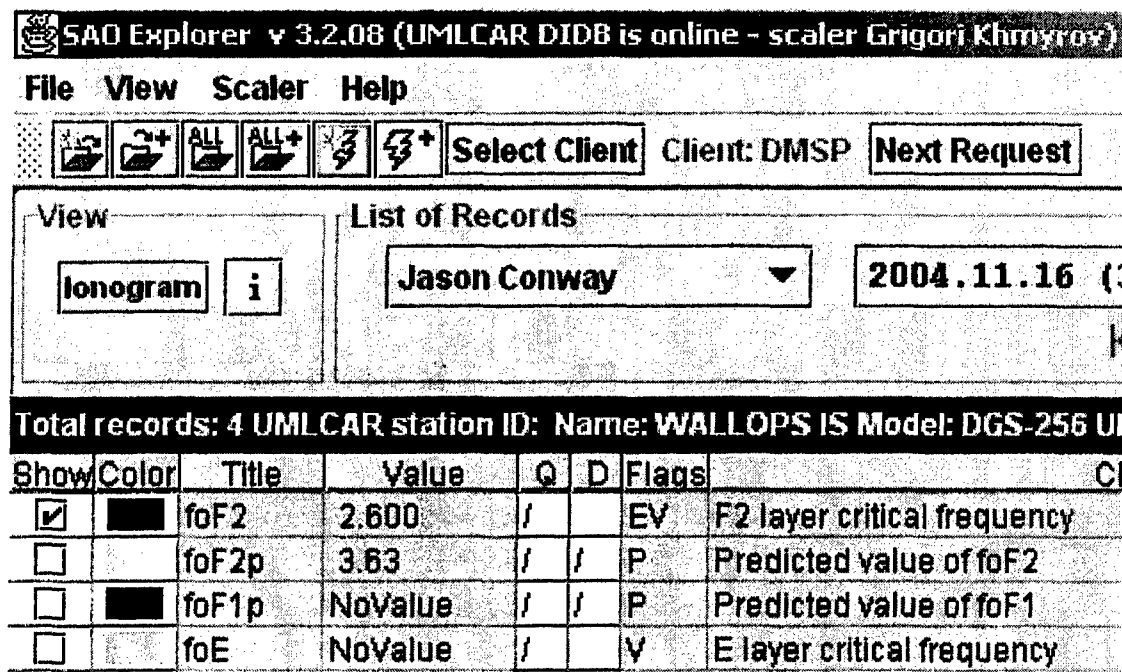
Figure 39. Part of the SAOExplorer Main Screen with "Next Request" Button

UMLCAR continues to support "future campaign mode". For this mode digisondes have to be switched to high cadence observations. Some digisonde software was reworked.

**7.1.1.1 DGS-256:**
DARTIST program
Dispatcher program
ProgSched file

**7.1.1.2 DPS-4:**
Dispatcher program
ProgSched file

A software status report was given during the CalVal meeting at NRL in November 2003.

### 8.3    CaVal results statistic

In January 2004, UMLCAR started receiving real time requests files. Most of them request regular F-layer manual scalings.

In addition to regular requests, another type of processing was used that analyzes the auroral E layer profiles. The auroral E requests include 19-20 February 2004 with a 5 min cadence for the ionograms from the Sondrestrom digisonde. For this analysis, full use has been made of the new SAO 4.3 format that supports auroral profiles and the DIDBase possibility to store multiple traces for E region echoes, which is important for the complex polar ionosphere.

Table 3 shows the status of data requests for the whole period since 1 January 2004 until September 30 2004.

**Table 3.  CalVal Digisonde Data Request Status**

| Request status | Total since 1 January 2004 |
|---|---|
| Total requests | 11777 |
| Requests loaded to DIDBase | 10498 |
| Requests not loaded (ADRES system is waiting for data availability) | 896 |
| Not available (no data) requests | 382 |
| Loaded but not scaled requests | 405 |
| Scaled and reported requests | 10038 |
| Scaled and reported ionograms | 37518 |

## 7.4 DIDBase improvements

In continuation of the CalVal project UMLCAR continues to build the DIDBase archive with most data loaded in real time.

**Online stations sending real-time data to DIDBase:**
(**bold** = non-DISS digisonde stations)

| | |
|---|---|
| **AN438** | **ANYANG** |
| AS00Q | ASCENSION ISLAND |
| **AT138** | **ATHENS** |
| **BC840** | **BOULDER** |
| **BV53Q** | **BUNDOORA** |
| CO764 | COLLEGE AK |
| **DB049** | **DOURBES** |
| DS932 | DYESS AFB |
| EG931 | EGLIN AFB |
| **EA036** | **EL ARENOSILLO** |
| FF051 | FAIRFORD |
| **GA762** | **GAKONA** |
| GSJ53 | GOOSE BAY |
| **GR13L** | **GRAHAMSTOWN** |
| **JI91J** | **JICAMARCA** |
| JR055 | JULIUSRUH |
| KS759 | KING SALMON |
| KJ609 | KWAJALEIN |
| LM42B | LEARMONTH |
| **LV12P** | **LOUISVALE** |
| **MU12K** | **MADIMBO** |
| **MHJ45** | **MILLSTONE HILL** |
| NQJ61 | NARSSARSSUAQ |
| SN437 | OSAN |
| **PQ052** | **PRUHONICE** |
| PA836 | PT ARGUELLO |
| THJ77 | QAANAAQ |
| PRJ18 | RAMEY |
| **EB040** | **ROQUETES** |
| T139 | SAN VITO |
| SMJ67 | SONDRESTROM |
| **TR169** | **TROMSO** |
| WP937 | WALLOPS IS |

**Stations reached by ADRES subsystem:**

| | |
|---|---|
| CAJ2M | CACHOEIRA PAULISTA |
| FZA0M | FORTALEZA |
| PRJ18 | ROME |
| SAA0K | SAO LUIS |

**Stations that are loaded manually:**

| | |
|---|---|
| RL052 | CHILTON |
| HA419 | HAINAN |
| IR352 | IRKUTSK |
| NO369 | NORILSK |
| PSJ5J | PORT STANLEY |
| TUJ20 | TUCUMAN |
| WU430 | WUHAN |
| YA462 | YAKUTSK |
| ZH466 | ZHIGANSK |

**Stations currently off:**

| | |
|---|---|
| OK426 | OKINAWA |
| TO535 | KOKUBUNJI |
| HAJ43 | HANSCOM AFB |
| BJJ32 | BERMUDA |

Because of the increasing size of DIDBase (at the moment ~ 110 GB), the DIDBase system storing ionograms, scaled and edited for the CalVal campaigns, has been extended from a 140 GB SCSI RAID-5 disc array to a 7 disc array with size 210 GB. In addition, a new backup server with 750 GB capacity was installed.

A special effort has been made to create a WEB interface to DIDBase by installing a new server with Tomcat WEB Application support. A number of "servlet" programs were written and installed on the server. The home page is http://umlcar.uml.edu/DIDBase/ (Figure 40)
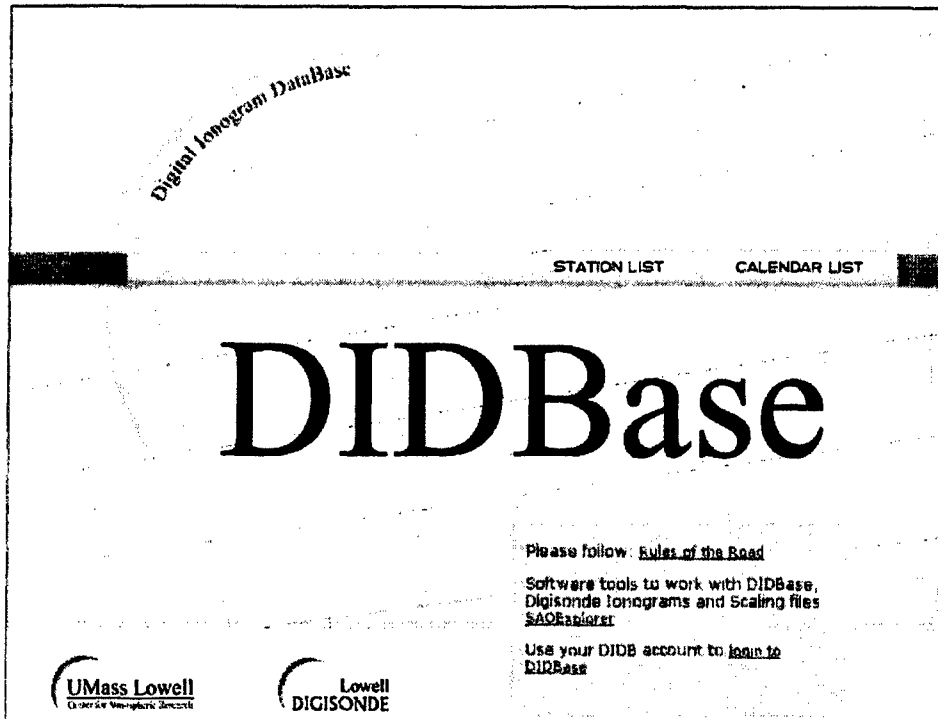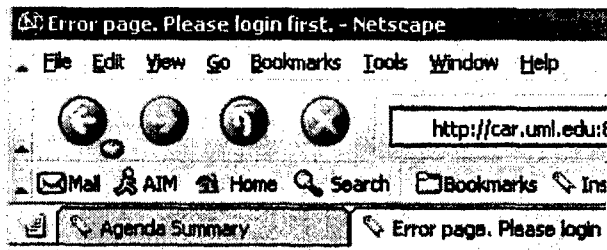
**Figure 40. The WEB Server Supports DIDBase Inventory Information and Ionogram Visualization.**
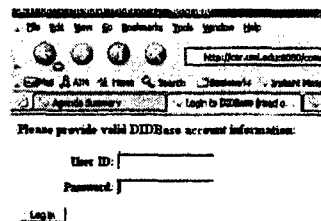
For registered users it is possible to see any ionogram from the DIDBase after "Login":

**Step 1**



Please login fist with valid DIDBase account.

**Step 2**

UMLCAR continues to produce manual scaling of the DIDBase data. Currently the total manually scaled data in DIDBase is about 150000 records (more than 4 years of 15 min data).

## 8    AUTOSCALING REFINEMENTS

### 8.1    Release of ARTIST 4.5 software

The quality of the ARTIST autoscaling continued to be our concern since the introduction of the ARTIST 4.0 version 0702 in the early 2003. By the middle of 2004, the total number of implemented improvements became significant enough to release a new version of the ARTIST 4.5 [Reinisch *et al.*, 2004b].

The largest deficiencies in the ARTIST 4.0 autoscaling were caused by premature truncation of the scaled F2 trace resulting in far too low foF2 values as illustrated in Figure 41a. The algorithm stopped scaling the echoes at 5.2 MHz, confused by the echo trace gaps near 5.5, 6.5 and 7.5 MHz. Aggravating the autoscaling task is the large number of "restricted frequencies" that are responsible for gaps in the ionogram traces. This problem is very severe at several digisonde stations of the DISS network, and also at Millstone Hill (42°N) as illustrated in Figure 41. The horizontal bar-underscores on the frequency axis indicate the restricted frequency bands.

Improvements in the trace gap bridging are typically sought by strengthening perceptual grouping qualities of the tracing algorithm [e.g., Galkin *et al.*, 2004]. We have realized, however, that trace extrapolation and interpolation through large gaps (e.g., a missing or weak F1 trace) can best be accomplished, and with a greater robustness, in the true height domain by reverse inversion (from trace segments to profile and from the calculated

59

profile back to the completed traces) [Reinisch and Huang, 1983]. Interpolation in the true height domain is a simpler task because of smaller gradients in the true height (or profile) domain, and it avoids creating non-physical trace segments that could not be produced by any plasma distribution.

The new ARTIST 4.5 version eliminates many of the "silly" mistakes of version 4.0, especially with regard to the handling of trace gaps and F2 trace truncations. A combination of simple coding errors and weaknesses in the algorithms in ARTIST 4.0 led to trace truncations as illustrated in Figure 41 that are now avoided with ARTIST 4.5. We use Millstone Hill ionograms for this illustration because of the many restricted frequencies. Figure 40a shows the ARTIST 4.0 (top) and 4.5 (middle) scalings for a nighttime ionogram, 40b for a daytime ionogram.
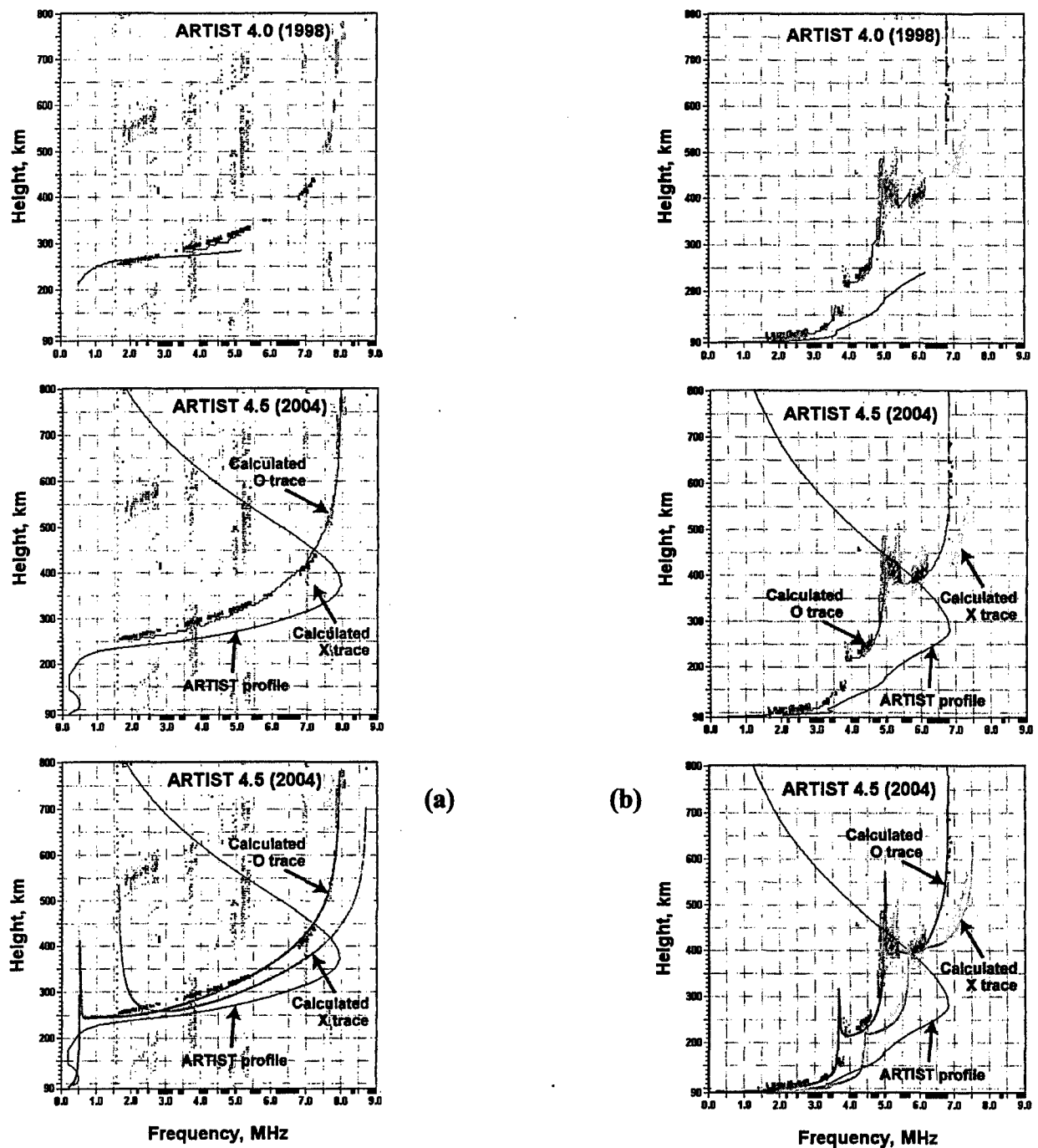
Figure 41. (a). Improved Nightttime ARTIST 4.5 Scaling (Middle Panel) Through Echo Trace Gaps, Caused by Transmission Restrictions and Interference, at Millstone Hill at 00 LT. The Marker Below the Horizontal Axis Indicates the Restricted Frequencies. The Top Panel Shows the Result of ARTIST 4.0 Scaling. The Bottom Panel Shows the Traces Calculated from the ARTIST 4.5. These Calculated $h'(f)$ Curves Coincide Almost Exactly with the Measured Echo Traces Confirming the Accuracy of the Autoscaling and the True Height Inversion Procedure of ARTIST. A Model is Used for the E and E-F Valley Region. (b) Same for Daytime, 15 LT.

61

To verify the reasonableness of the scaling and profile inversion, the true height inversion program NHPC [Huang and Reinisch, 2001] calculated the O and X ionogram traces in a forward inversion of the obtained profile (continuous curves in the bottom panel). These recalculated traces are a very good replica of the measured O and X echo points. The reasonably good match obtained with ARTIST 4.5 of the recalculated traces with the measured ones instills confidence in the automated ionogram processing. The topside profiles in Figure 41 are automatically calculated using the Reinisch–Huang technique. An α-Chapman distribution is assumed with a constant scale height $H_T$ that is derived from the measured bottomside profile [Reinisch and Huang, 2001]. The SAO-Explorer generated "profilograms" (Figure 42) display both bottomside and topside density profiles as function of height (90 – 1000 km) and time. The comparison of profilograms based on autoscaled ARTIST 4.5 and manually edited traces in Figure 42 gives confidence to the use of ARTIST scaled data. Though certainly superior in quality of trace extraction, the manual validation venue is not available for real time assimilation tasks.



**ARTIST 4.5**                                    **Manual Scaling**

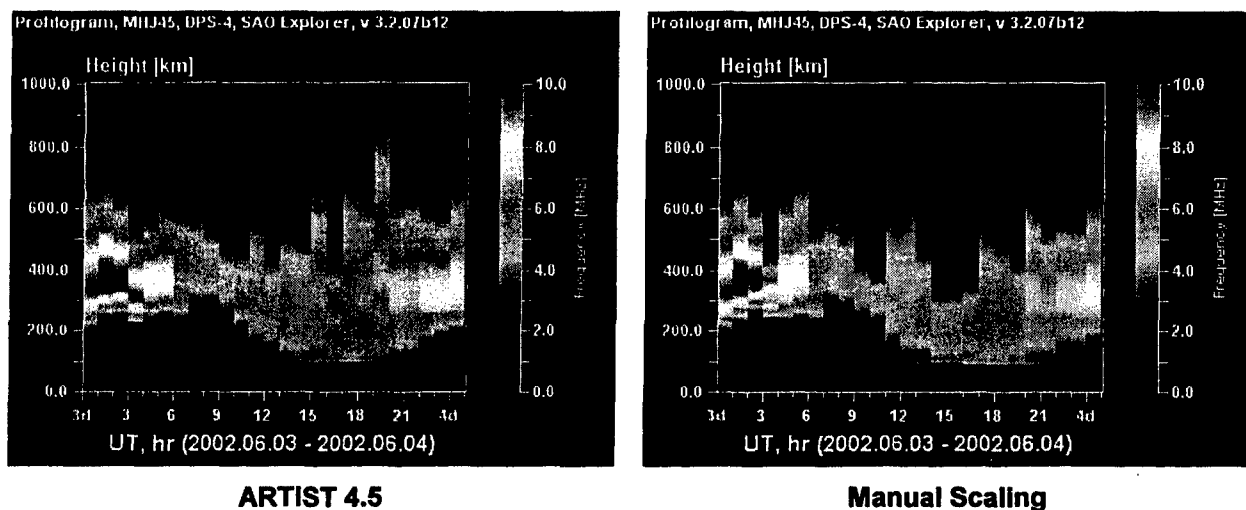Figure 42. SAO-Explorer Profilograms Show Electron Density (or Plasma Frequency) as Function of Height and Time. Comparison of ARTIST 4.5 (Left) and Manually (Right) Scaled Data Reveals the Usefulness of ARTIST Scaled Profile Data.

Many stations operate without severe frequency restrictions but trace gaps can still occur as discussed above. Analysis of data from such locations confirmed a greater quality of

ionogram scaling by ARTIST 4.5. To quantitatively assess the performance of ARTIST 4.5 in comparison to ARTIST 4.0, all scalable half-hour ionograms from Millstone Hill, Boulder, and Athens digisondes were manually scaled for one month and compared with the autoscaled results. As a performance measure we used the foF2 values and plotted the deviations ΔfoF2 (Figure 43) demonstrating that the number of foF2 errors above 0.2 MHz is dramatically reduced. The cumulative relative ΔfoF2 differences plotted in Figure 44 show the improvement even better. For Boulder and Athens the improvements are less dramatic (not shown here) because of the absence of frequency restrictions in these digisondes, however the observed increases from 85% to 95% (Athens) and from 82% to 94% (Boulder) of foF2 scalings within 0.2 MHz accuracy are still significant.
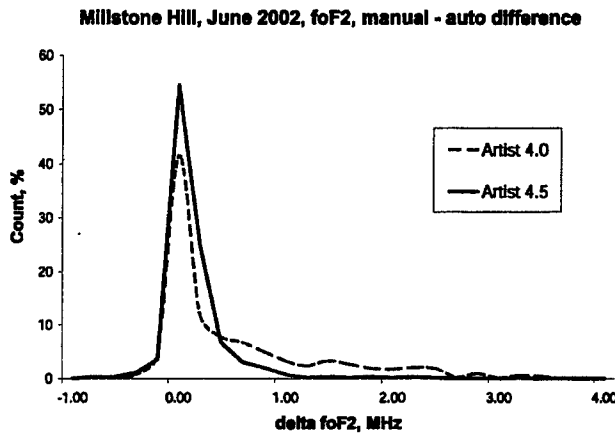


Figure 43. Errors ΔfoF2 for ARTIST 4.0 and 4.5 for Millstone Hill, June 2002.
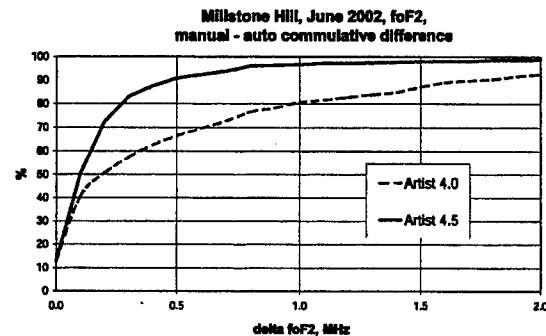
Figure 44. Relative Cumulative ΔfoF2 Distribution for Millstone Hill, June 2002.

## 8.2    Study of ARTIST profile uncertainty

Kalman-filter data assimilation models are expected to become the most promising technique for space weather applications following their success in meteorology and oceanography after several decades of research. New ionospheric assimilation models like the Global Assimilation of Ionospheric Measurements (GAIM) [Schunk et al., 2004] differ from prior generation adaptive ionospheric models in that they analyze the

63

uncertainty of the observational inputs before using them as constraints on the physical model drivers. These uncertainties are important for the Kalman filter to dynamically evolve into an optimal state where model and observations are matched with the least error.

In September 2004 we started a new project of upgrading ARTIST software to automatically determine the uncertainty of each $N(h)$-profile point, i.e., to specify $\Delta N$ at each height. To calculate point-by-point uncertainties, two boundary profiles, inner and outer, will be determined to define the uncertainty range (Figure 45). The inner and outer boundaries will reflect point-by-point uncertainties of the scaled virtual heights $\Delta h'(f)$ and critical frequencies $\Delta f_{cr}$ of each layer, internal uncertainty of the starting height of the profile, and uncertainties of the E valley model representation. We are actively establishing a reference database of manually scaled ionograms that will be used to evaluate typical scaling uncertainties. We selected a few digisondes that operate properly (well calibrated, no faulty hardware, optimal settings) and extend the results to other digisondes.
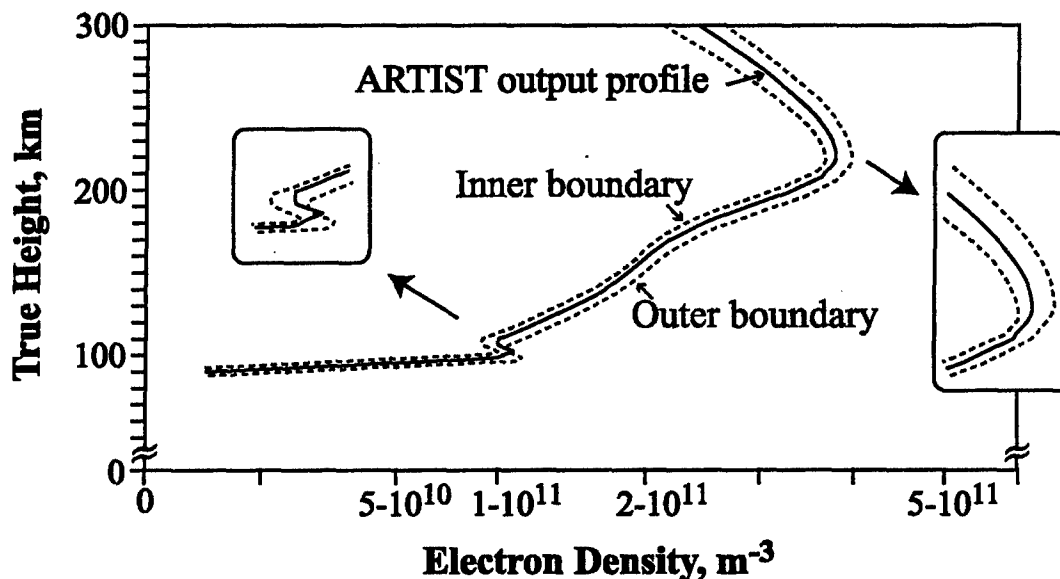


Figure 45. The Profile Uncertainty is Specified by Inner and Outer Boundary Profiles (Cartoon)

In addition, the profile uncertainties will be combined with an autoscaling confidence level for the entire profile to assist top-level decisions to accept or reject the profile for assimilation. The confidence level shall reflect the complexity of the ionogram (spread F, ionospheric tilt, blanketing Es, absorption, etc.) and the ionogram quality based on signal-to-noise ratios and station performance history.

# 9    LIST OF PUBLICATIONS AND PRESENTATIONS

Bernhardt, P. A., P. J. Erickson, F. D. Lind, J. C. Foster and B. W Reinisch, Artificial Disturbances of the Ionosphere over the Millstone Hill Incoherent Scatter Radar During Dedicated Burns of the Space Shuttle OMS Engines, submitted, *J. Geophys. Res.*, 2004.

Reinisch, B. W., M. Abdu, I. Batista, G. S. Sales, G. Khmyrov, T. A. Bullett, J. Chau, and V. Rios, Multistation digisonde observations of equatorial spared F in South America, *Annales Geophysicae*, 22: 1-9, 2004.

Reinisch, B. W., X. Huang, I. A. Galkin, V. Paznukhov, and A. Kozlov, Recent advances in real-time analysis of ionograms and ionospheric drift measurements with digisondes, submitted, *Journal of Atmospheric and Solar-Terrestrial Physics, 2004.*

Reinisch, B. W., I. A. Galkin, G. Khmyrov, A. Kozlov, and D. F. Kitrosser, Automated collection and dissemination of ionospheric data from the digisonde network, *Adv. Radio Sci.*, 2: 241-247, 2004.

Reinisch, B. W., X. Huang, A. Belehaki, and R. Ilma, Using scale heights derived from bottomside ionograms for modeling the IRI topside profile, *Adv. Radio Sci.*, 2: 293-297, 2004.

Reinisch, B. W., Tenth International Digisonde Training Seminar at UMass Lowell Reviews State of Real Time Mapping of the Ionosphere, IEEE A & P Magazine, 2004.

Reinisch, B. W. and D. Bilitza, Karl Rawer's Life and the History of IRI, *Adv. in Radio Sci.,* 2004.

Abdu, M. A., T. K. Ramkumar, I. S. Batista, C. G. M. Brum, H. Takashashi, B. W. Reinisch, and J. H. A. Sobral, Mesosphere-E-and F-Region Coupling, and Planetary Wave Effects in the Equatorial Ionosphere, *J. Atmos. and Solar Terr. Physics*, 2004.

AGU Western Pacific Mtg. - Honolulu, HI – Session SA02/Variability of the Equatorial Ionosphere and effects on Radio Systems- August 2004 (convener: B. Reinisch)

- The coupling factor of the ionosphere for the VLF waves, P. Song, G. Sales, V. Paznukhov, B. Reinisch, and I. Galkin

- Formation of F-region irregularities along magnetic equator during S. America COPEX campaign, G. Sales, B. Reinisch, M. Abdu, and I. Batista
- Equatorial ionosphere variability in Brazil: Results from conjugate point equatorial experiments campaign (COPEX), I. S. Batista, M. A. Abdu, B. W. Reinisch, F. Bertoni, J. R. de Souza, E. R. dePaula, K. Groves, T. W. Bullett, and J. H. A. Sobral
- Ionospheric Plasma Drift Characteristics Observed in Hainan, J. K. Shi, X. Wang, S.Z. Wu, and B. W. Reinisch

COSPAR - Paris, July 2004

- Deducing an IRI topside profile from the IRI bottomside profile, Bodo W. Reinisch and Xueqin Huang
- Diurnal and Seasonal Variation of the Scale Height at F2 Peak Altitude for Hainan, M. L. Zhang, J. K. Shi, X. Wang, B. W. Reinisch

EGU 2004, 1st General Assembly - Nice, France, April 2004
- Recent advances in real time analysis of ionograms and F region drift, B. W. Reinisch, X. Huang, V. Paznukhov, and A. Kozlov

2004 AGU Joint Assembly (SPA-Aeronomy)
- A one-dimensional ionosphere solution with self-consistent neutral motion, P. Song and V. Vasyliunas

2004 AGU Meeting – Montreal, Canada
- Equatorial Spread F Variability Investigations in Brazil: Preliminary Results from Conjugate Point Equatorial Experiments Campaign – COPEX, M. A. Abdu, I. S. Batista, B. W. Reinisch, J. R. de Souza, E. R. de Paula, J. H. A. Sobral and T. W. Bullet

2004 URSI National Radio Science Meeting

- Observations of the Inner Magnetospheric and Radiation Belt Processes by Radio Plasma Imager on IMAGE, B. W. Reinisch, P. Song, X. Huang, and J. Green
- Measuring whistler mode signals in the magnetosphere originating from ground-based VLF transmitters using the IMAGE/RPI satellite, G. S. Sales V. Paznukhov, P. Song, B.W. Reinisch, G. Khmyrov
- Irregularity Formation at Cachimbo on the Magnetic Equator after sunset during the COPEX campaign in Brazil, G. Sales, B. Reinisch, M. Abdu, and I. Batista

# 10    REFERENCES

Belmain, K.G., The impedance of a short dipole antenna in a magnetoplasma, *IEEE, Trans. Antennas Propag.*, 12, 605, 1964.

Djuth, Frank D., B. W. Reinisch, D. S. Kitrosser, A. Lee Snyder, and G. S. Sales, Imaging HF induced irregularities of HAARP, to be submitted, *Geophys. Res. Ltrs.*, 2005.

Galkin, I. A., B. W. Reinisch, G. Grinstein, G. M. Khmyrov, A. Kozlov, X. Huang, and S. F. Fung, Automated Exploration of the Radio Plasma Imager Data, in press, *J. Geophys. Res.*, November 2004.

Huang, X. and B. W. Reinisch, Vertical Electron Content from Ionograms in Real Time, *Radio Sci.*, 36, 2, 335-342, March/April 2001.

Oliver, B. M., R. M. Clements, and P. R. Smy, Experimental investigation of the low-frequency capacitive response of a plasma sheath, *J. Appl. Phys.*, 44, 4511, 1973

Reinisch, B. W. and X. Huang, Automatic Calculation of Electron Density Profiles from Digital Ionograms, 3, Processing of Bottomside Ionograms, *Radio Sci.*, 18, 477-492, 1983.

Reinisch et al., The Radio Plasma Imager investigation on the IMAGE spacecraft, *Space Sci. Reviews*, **91**, 319-359, 2000.

Reinisch, B. W., M. Abdu, I. Batista, G. S. Sales, G. Khmyrov, T. A. Bullett, J. Chau, and V. Rios, Multistation digisonde observations of equatorial spared F in South America, *Annales Geophysicae*, 22: 1-9, 2004a.

Reinisch, B. W., I. A. Galkin, G. Khmyrov, A. Kozlov, and D. F. Kitrosser, Automated collection and dissemination of ionospheric data from the digisonde network, *Adv. Radio Sci.*, 2: 241-247, 2004b.

Reinisch, B. W., I. A. Galkin, G. Khmyrov, A. Kozlov, and D. F. Kitrosser, Automated collection and dissemination of ionospheric data from the digisonde network, *Adv. Radio Sci.* 2: 241-247, 2004c.

Reinisch, B. W., X. Huang, I. A. Galkin, V. Paznukhov, A. Kozlov, Recent advances in real-time analysis of ionograms and ionospheric drift measurements with digisondes, in press, *J. Atmos. Solar-Terr. Physics*, 2004d.

Reinisch, B. W., X. Huang, K. McCarthy, Real time raytracing through measured Ne profiles in the presence of ionospheric tilts, *Proc. USNC URSI, Boulder Co.*, January, 2005.

Sales, G.S., B.W. Reinisch, J.L. Scali, C. Dozois, T.W. Bullett, E. J. Weber, and P. Ning, Spread-F and the structure of equatorial ionization depletions in the Southern Anomaly Region, *J. Geophys. Res.*, 101, A12, 26,819-26,827, 1996.

Schunk, Robert W. et al., Global Assimilation of Ionospheric Measurements (GAIM), *Radio Sci.*, 39, RS1S02, doi:10.1029/2002RS002794, 2004.

Shkarofsky, I.P., Nonlinear sheath admittance, currents, and charges associated with high peak voltage drive on a VLF/ELF dipole antenna moving in the ionosphere, *Radio Sci.*, 7, 4, 503-523, 1972